Petroleum Science 21 (2024) 252–271

Contents lists available at ScienceDirect

Petroleum Science

journal homepage: www.keaipublishing.com/en/journals/petroleum-science

Original Paper

Linearized waveform inversion for vertical transversely isotropic elastic media: Methodology and multi-parameter crosstalk analysis

Ke Chen [a], Lu Liu [b], Li-Nan Xu [c], Fei Hu [d], Yuan Yang [d], Jia-Hui Zuo [a], Le-Le Zhang [a], Yang Zhao [a, *]

[a] National Key Laboratory of Petroleum Resources and Engineering, Unconventional Petroleum Research Institute, China University of Petroleum (Beijing), Beijing, 102249, China
[b] Aramco Beijing Research Center, Aramco Asia, Beijing, 100102, China
[c] University of Lausanne, Lausanne, CH-1015, Switzerland
[d] Bureau of Geophysical Prospecting, China National Petroleum Corporation, Zhuozhou 072750, Hebei, China

ARTICLE INFO

Article history:
Received 21 November 2022
Received in revised form
12 December 2023
Accepted 2 January 2024
Available online 8 January 2024

Edited by Jie Hao and Meng-Jiao Zhou

Keywords:
Elastic
Anisotropy
Least-squares imaging
Waveform inversion
Computational geophysics

ABSTRACT

Seismic migration and inversion are closely related techniques to portray subsurface images and identify hydrocarbon reservoirs. Seismic migration aims at obtaining structural images of subsurface geologic discontinuities. More specifically, seismic migration estimates the reflectivity function (stacked average reflectivity or pre-stack angle-dependent reflectivity) from seismic reflection data. On the other hand, seismic inversion quantitatively estimates the intrinsic rock properties of subsurface formulations. Such seismic inversion methods are applicable to detect hydrocarbon reservoirs that may exhibit lateral variations in the inverted parameters. Although there exist many differences, pre-stack seismic migration is similar with the first iteration of the general linearized seismic inversion.

Usually, seismic migration and inversion techniques assume an acoustic or isotropic elastic medium. Unconventional reservoirs such as shale and tight sand formation have notable anisotropic property. We present a linearized waveform inversion (LWI) scheme for weakly anisotropic elastic media with vertical transversely isotropic (VTI) symmetry. It is based on two-way anisotropic elastic wave equation and simultaneously inverts for the localized perturbations $(\Delta V_{p0}/V_{p0}, \Delta V_{s0}/V_{s0}, \Delta\epsilon, \Delta\delta)$ from the long-wavelength reference model. Our proposed VTI-elastic LWI is an iterative method that requires a forward and an adjoint operator acting on vectors in each iteration. We derive the forward Born approximation operator by perturbation theory and adjoint operator via adjoint-state method. The inversion has improved the quality of the images and reduces the multi-parameter crosstalk comparing with the adjoint-based images. We have observed that the multi-parameter crosstalk problem is more prominent in the inversion images for Thomsen anisotropy parameters. Especially, the Thomsen parameter δ is the most difficult to resolve. We also analyze the multi-parameter crosstalk using scattering radiation patterns.

The linearized waveform inversion for VTI-elastic media presented in this article provides quantitative information of the rock properties that has the potential to help identify hydrocarbon reservoirs.

1. Introduction

Seismic migration locates subsurface reflectors where the Earth properties are rapidly changed, which can be used to make inferences about the location and quantity of hydrocarbons. Reverse time migration (RTM) continues a wave from source forward in time and continues reflection data backward in time and estimates the reflectivity function by zero-lag cross-correlating the two wavefields. Modern RTM algorithms have also incorporated elasticity for imaging complex subsurface structures (Du et al., 2012; Zhang and Shi, 2019; Zhong et al., 2021). In elastic RTM, P- and S-wave separation is an important step to reduce wave-mode crosstalk in migrated images (Yan and Sava, 2008; Cheng and Fomel,

* Corresponding author.
E-mail address: zhaoyang@cup.edu.cn (Y. Zhao).

https://doi.org/10.1016/j.petsci.2024.01.002

2014; Li et al., 2016; Yang et al., 2018a). Unconventional reservoirs such as shale or tight sand formation has notable anisotropic property. The anisotropic constitutive model means that properties of the earth at any spatial point are directionally dependent. The mechanism of macroscopic scale anisotropy includes preferred orientation of crystals, periodic-thin layering, and aligned cracks/pores/impurities (Musgrave, 2003). Considering anisotropy poses new complexities and challenges to seismic imaging (Lu et al., 2019; Wang and Zhang, 2022; Zuo et al., 2022; Zhong et al., 2022). The main bottleneck in anisotropic elastic RTM is how to efficiently separate P- and S-wave to avoid wave-mode crosstalk in images (Zhang and McMechan, 2010; Cheng and Fomel, 2014; Wang et al., 2016, 2021; Yang et al., 2019a; Zhang et al., 2022).

Seismic migration solves the reflectivity function at each subsurface point by applying linear operator on seismic reflection data. Note that, the reflectivity is not an intrinsic Earth property but a function of both rock mechanical properties and the directions of incident/reflected waves. On the other hand, linearized inversion quantitatively estimates the intrinsic rock mechanical properties (Tarantola, 1984; Bourgeois et al., 1989; Lambaré et al., 1992; Østmo et al., 2002). The perturbations of velocity, slowness or acoustic impedance are parameters inverted from the seismic reflection data. Later, the linearized inversion theory is further developed under the name of least-squares migration (Nemeth et al., 1999; Kuehl and Sacchi, 2003; Huang et al., 2013; Yao and Jakubowicz, 2016; Yang et al., 2016; Lu et al., 2017; Li et al., 2018). In acoustic media, the terminology of linearized inversion and least-squares migration are interchangeably used because the inverted model parameter perturbation and the inverted stacked images have a one-to-one mapping relationship. However, the two techniques are essentially different that their results have different physical meanings. The angle/source/offset dependent image volume estimated in least-squares migration is a combination of both model parameter perturbations and spatial differential operators (or local wavenumber vectors).

For isotropic elastic media, linearized inversion simultaneously inverts for multiple elastic parameters such as P- and S-wave impedance/velocity perturbations or Lamé parameter perturbations, may or may not include density perturbation (Anikiev et al., 2013; Feng and Schuster, 2017; Duan et al., 2017; Chen and Sacchi, 2017, 2018; Ren et al., 2017; Gu et al., 2017; Qu et al., 2019; Sun et al., 2018; Fang et al., 2019). In these studies, the intrinsic rock mechanical properties are estimated instead of the angle-dependent reflectivity. On the other hand, Stanton and Sacchi (2017) presented an elastic least-squares one-way wave equation migration method based on Helmholtz decomposition to estimate PP and PS images from multicomponent seismic data (Xu et al., 2016). Gu et al. (2019, 2021) presented an elastic least-squares reverse time migration (LSRTM) based on elastic wavefield decomposition to simultaneously map the PP and PS images. In those studies, the PP and PS wave images are estimated from the reflection seismic data that represent angle-dependent reflectivity coefficients. For isotropic elastic media, the linearized inversion and least-squares migration are essentially different. However, the difference is often overlooked in literatures of seismic imaging and inversion.

The exploration and exploitation of complex oil and gas reservoirs requires the development of high-resolution imaging technique for anisotropic elastic media. Considering anisotropy in seismic imaging and inversion techniques provides potentials to reveal information related to mineral orientation, fine stratification, stress state and fracturing. This article deals with linearized waveform inversion in the presence of anisotropy in elastic media. In previous works, Yang et al. (2019b) proposed an elastic LSRTM method in VTI media by solving the elastic stiffnesses perturbations (ΔC_{33} and ΔC_{55}) as PP and PS images. In a similar vein, Yang et al. (2020) investigated an elastic LSRTM in tilted transversely isotropic (TTI) media using elastic stiffnesses perturbations $\Delta\ln C_{33}$ and $\Delta\ln C_{55}$ as PP and PS images, respectively. From a different point of view, Chen et al. (2023) proposed a VTI-elastic LSRTM based on elastic wavefield vector decomposition which simultaneously inverts for PP, PS, SP and SS reflectivity images. Mu et al. (2020) studied a LSRTM algorithm for TTI-acoustic media based on TTI pure qP-wave equation.

In this article, we develop a linearized waveform inversion (LWI) for VTI-elastic media based on anisotropic elastic wave equation and Born approximation. Different from seeking for PP, PS, SP and SS reflectivity images (Chen et al., 2023), our method inverts for the distribution of localized perturbations from the background rock mechanical property model ($\Delta V_{p0}/V_{p0}$, $\Delta V_{s0}/V_{s0}$, $\Delta\epsilon$, $\Delta\delta$). Our method is also different from Yang et al. (2019b) in that we simultaneously invert for the velocities and anisotropic parameters and analyze the multi-parameter crosstalk in anisotropic elastic waveform inversion based on ray-Born approximation. In addition, we point out the differences and connections between least-squares migration and linearized waveform inversion which is commonly overlooked in seismic imaging/inversion community. We observe that the multi-parameter crosstalk issue is more prominent in the inversion results for anisotropy parameters. And the Thomsen parameter δ is the most difficult one to resolve. The inversion results of anisotropy parameters are also more easily influenced by observation data noise and reference model error. The multi-parameter crosstalk analysis based on ray-Born approximation partially explain this phenomenon.

We summarize the novelty of the paper and our contributions as follows: First, we develop the mathematical basis for linearized waveform inversion in anisotropic elastic media based on full anisotropic elastic wave equation. Second, we formally point out the differences and connections between least-squares migration and linearized waveform inversion. Third, we simultaneously invert for localized perturbations of petrophysical parameters ($\Delta V_{p0}/V_{p0}, \Delta V_{s0}/V_{s0}, \Delta\epsilon, \Delta\delta$) instead of seeking for the PP, PS, SP and SS reflectivity images. Fourth, we utilize the ray-Born approximation method to estimate the scattering radiation patterns to analyze the multi-parameter crosstalk in LWI for VTI-elastic media.

This paper is organized as follows: First, we review the anisotropic elastic wave equation and derive its Born approximation formulations. Subsequently, we pose a linear least-squares inverse problem based on the linearized Born approximation operator. The solution of the inversion is sought using the conjugate gradient method. Finally, we present a series of numerical tests using synthetic data. In Appendices, we present the derivation of the adjoint operator and multi-parameter crosstalk analysis based on scattering radiation patterns of anisotropic elastic parameters.

2. Method

2.1. The linearized forward problem in VTI-elastic media

We start the derivation of the method from a general forward problem for seismic waves in a VTI-elastic media. The propagation

of seismic wave satisfies the equations of motion, subject to appropriate boundary conditions:

$$\begin{aligned}
&\rho\frac{\partial v_1}{\partial t}-\left(\frac{\partial \sigma_{11}}{\partial x_1}+\frac{\partial \sigma_{13}}{\partial x_3}\right)=f_1,\\
&\rho\frac{\partial v_3}{\partial t}-\left(\frac{\partial \sigma_{13}}{\partial x_1}+\frac{\partial \sigma_{33}}{\partial x_3}\right)=f_3,\\
&\frac{\partial \sigma_{11}}{\partial t}-C_{11}\frac{\partial v_1}{\partial x_1}-C_{13}\frac{\partial v_3}{\partial x_3}=0,\\
&\frac{\partial \sigma_{33}}{\partial t}-C_{13}\frac{\partial v_1}{\partial x_1}-C_{33}\frac{\partial v_3}{\partial x_3}=0,\\
&\frac{\partial \sigma_{13}}{\partial t}-C_{55}\left(\frac{\partial v_1}{\partial x_3}+\frac{\partial v_3}{\partial x_1}\right)=0,
\end{aligned} \tag{1}$$

here, (v_1, v_3) are horizontal and vertical particle velocities, $(\sigma_{11}, \sigma_{33}, \sigma_{13})$ are stress components, (f_1, f_3) are body forces, ρ is the density, C_{ij} are elements of the stiffness matrix. This paper is concerned with weak elastic anisotropy (Thomsen, 1986), and elastic stiffnesses can be expressed as

$$\begin{aligned}
&C_{33}=\rho V_{p0}^2, C_{55}=\rho V_{s0}^2, C_{11}=(1+2\epsilon)C_{33},\\
&C_{13}=\sqrt{[(1+2\delta)C_{33}-C_{55}](C_{33}-C_{55})}-C_{55},
\end{aligned} \tag{2}$$

where V_{p0} and V_{s0} are vertical velocities for P- and S-waves, ϵ and δ are Thomsen anisotropy parameters. We reformulate the elastic wave equation (Eq. (1)) to the following system of equations (Yang et al., 2018b):

$$\begin{cases}
\rho\dfrac{\partial \mathbf{v}}{\partial t}-\mathbf{D}\boldsymbol{\sigma}=\mathbf{f}_a,\\
\dfrac{\partial \boldsymbol{\sigma}}{\partial t}-\mathbf{C}\mathbf{D}^{\mathrm{T}}\mathbf{v}=\mathbf{0},
\end{cases} \tag{3}$$

where

$$\mathbf{v}=\begin{pmatrix} v_1\\ v_3\end{pmatrix},\ \boldsymbol{\sigma}=\begin{pmatrix}\sigma_{11}\\ \sigma_{33}\\ \sigma_{13}\end{pmatrix},\ \mathbf{C}=\begin{pmatrix} C_{11} & C_{13} & 0\\ C_{13} & C_{33} & 0\\ 0 & 0 & C_{55}\end{pmatrix},\quad \mathbf{D}=\begin{pmatrix}\dfrac{\partial}{\partial x_1} & 0 & \dfrac{\partial}{\partial x_3}\\ 0 & \dfrac{\partial}{\partial x_3} & \dfrac{\partial}{\partial x_1}\end{pmatrix}. \tag{4}$$

In the above equation, vector $\mathbf{v}$ represents particle velocity, vector $\boldsymbol{\sigma}$ indicates stress, matrix $\mathbf{C}$ denotes the stiffness matrix and matrix $\mathbf{D}$ contains spatial partial differential operators of the wave equation. Finally, $\mathbf{f}_a$ is the source vector applied on particle accelerations. More concisely, we can express the anisotropic elastic wave equation (Eq. (3)) as

$$\mathscr{A}\mathbf{u}=\mathbf{f}, \tag{5}$$

with

$$\mathscr{A}=\begin{pmatrix}\rho\mathbf{I} & \mathbf{0}\\ \mathbf{0} & \mathbf{I}\end{pmatrix}\frac{\partial}{\partial t}-\begin{pmatrix}\mathbf{0} & \mathbf{D}\\ \mathbf{C}\mathbf{D}^{\mathrm{T}} & \mathbf{0}\end{pmatrix},\quad \mathbf{u}=\begin{pmatrix}\mathbf{v}\\ \boldsymbol{\sigma}\end{pmatrix},\mathbf{f}=\begin{pmatrix}\mathbf{f}_a\\ \mathbf{0}\end{pmatrix}. \tag{6}$$

Note that, the elastic wave operator $\mathscr{A}$ depends on the model parameters ρ and $\mathbf{C}$ (i.e. $\mathscr{A}=\mathscr{A}_{[\rho,\ \mathbf{C}]}$). The seismic data recorded at the locations of seismic sensors are obtained by extracting seismograms from seismic wavefield via a sampling operator:

$$\mathbf{d}=\mathscr{R}\mathbf{u}, \tag{7}$$

where $\mathbf{d}$ denotes the observed seismic data and operator $\mathscr{R}$ represents the sampling operator. The seismic inverse problem entails inferring subsurface model parameters from the seismic data recorded at the earth surface. In mathematical jargon, the seismic inverse problem is to optimize the coefficients of the partial differential equations (PDEs) from the boundary measurements. This is the well-known full-waveform inversion (FWI) problem in geophysics community. High computational cost, local minima and multi-parameter crosstalk are among the main challenges for FWI (Virieux and Operto, 2009; Kohn, 2011). A less ambitious approach is the linearized waveform inversion (or Born inversion) that replaces the nonlinear wave equation modeling operator by the linearized Born approximation modeling operator and solves for localized perturbations with respect to the reference model (Tarantola, 1984; Bourgeois et al., 1989). It does not seek to resolve the entire wavelength spectrum of the absolute model parameters. In this article, we present a linearized waveform inversion for VTI-elastic media and analyze the multi-parameter crosstalk in the inversion.

We derive the Born approximation by applying the perturbation theory to the anisotropic elastic wave equation. We assume that the values for reference model of elastic parameters are known and are required to be relatively smooth and continuous. Elastic wave propagation in the reference media (ρ^0, $\mathbf{C}^0$) is described by

$$\mathscr{A}^0\mathbf{u}^0=\mathbf{f}, \tag{8}$$

where $\mathscr{A}^0$ and $\mathbf{u}^0=(\mathbf{v}^0, \boldsymbol{\sigma}^0)^{\mathrm{T}}$ are reference elastic wave operator and reference elastic wavefield, respectively. Expanding the elastic wave operator using Eq. (6), we have

$$\begin{cases}
\rho^0\dfrac{\partial \mathbf{v}^0}{\partial t}-\mathbf{D}\boldsymbol{\sigma}^0=\mathbf{f}_a,\\
\dfrac{\partial \boldsymbol{\sigma}^0}{\partial t}-\mathbf{C}^0\mathbf{D}^{\mathrm{T}}\mathbf{v}^0=\mathbf{0},
\end{cases} \tag{9}$$

where $(\rho^0, \mathbf{C}^0)$ represents the reference background model. The process of linearization of elastic wave operator is achieved as follows. We assume a perturbation of the model with respect to a reference medium:

$$\begin{aligned}
&\rho^0\to\rho^0+\Delta\rho,\\
&\mathbf{C}^0\to\mathbf{C}^0+\Delta\mathbf{C},
\end{aligned} \tag{10}$$

with $(\Delta\rho, \Delta\mathbf{C})$ as model perturbation. The seismic wavefield disturbed by model parameters perturbation is

$$\mathbf{u}^0\to\mathbf{u}^0+\Delta\mathbf{u}. \tag{11}$$

Due to model perturbation, the elastic wave Eq. (8) changes to

$$\left(\mathscr{A}^0+\Delta\mathscr{A}\right)\left(\mathbf{u}^0+\Delta\mathbf{u}\right)=\mathbf{f}, \tag{12}$$

where $\Delta\mathscr{A}$ and $\Delta\mathbf{u}$ are the scattering potential and the scattered wavefield, respectively. The scattering potential is defined as the difference between the exact and reference wave operators (Stolt and Weglein, 2012). To only consider single scattering, we neglect second-order terms of small perturbations and apply the relationship $\mathscr{A}^0\mathbf{u}^0=\mathbf{f}$ to arrive

$$\mathscr{A}^0\Delta\mathbf{u} = -\Delta\mathscr{A}\mathbf{u}^0. \tag{13}$$

As mentioned above, the seismic seismograms are retrieved by sampling the wavefield at receiver locations. The scattered seismic data can be expressed as

$$\Delta\mathbf{d} = \mathscr{R}\Delta\mathbf{u} = -\mathscr{R}\left(\mathscr{A}^0\right)^{-1}\Delta\mathscr{A}\mathbf{u}^0 = -\mathscr{R}\left(\mathscr{A}^0\right)^{-1}\frac{\partial\mathscr{A}}{\partial\mathbf{m}}\mathbf{u}^0\Delta\mathbf{m}, \tag{14}$$

where $\left(\mathscr{A}^0\right)^{-1}$ is the inverse elastic wave operator, $\Delta\mathbf{m}$ is the model vector perturbation, the derivative of elastic wave operator with respect to model parameter ($\partial\mathscr{A}/\partial\mathbf{m}$) indicates the radiation pattern of the parameter (Kamath and Tsvankin, 2016).

Eq. (13) is abstract representation of the Born approximation for general wave equation. Inserting the expression for the elastic wave operator $\mathscr{A}^0$ and scattering potential $\Delta\mathscr{A}$ into Eq. (13), one can arrive the following system of partial differential equations:

$$\begin{cases} \rho^0\dfrac{\partial\Delta\mathbf{v}}{\partial t} - \mathbf{D}\Delta\boldsymbol{\sigma} = -\Delta\rho\dfrac{\partial\mathbf{v}^0}{\partial t}, \\ \dfrac{\partial\Delta\boldsymbol{\sigma}}{\partial t} - \mathbf{C}^0\mathbf{D}^{\mathrm{T}}\Delta\mathbf{v} = \Delta\mathbf{C}\mathbf{D}^{\mathrm{T}}\mathbf{v}^0, \end{cases} \tag{15}$$

where

$$\Delta\mathbf{v} = \begin{pmatrix}\Delta v_1\\ \Delta v_3\end{pmatrix},\ \Delta\boldsymbol{\sigma} = \begin{pmatrix}\Delta\sigma_{11}\\ \Delta\sigma_{33}\\ \Delta\sigma_{13}\end{pmatrix},\quad \Delta\mathbf{C} = \begin{pmatrix}\Delta C_{11} & \Delta C_{13} & 0\\ \Delta C_{13} & \Delta C_{33} & 0\\ 0 & 0 & \Delta C_{55}\end{pmatrix}. \tag{16}$$

Eq. (15) represents the first-order Born approximation for an anisotropic elastic wave equation. In the derived Born approximation equation, the model parameters are perturbations relative to the background medium in terms of elastic stiffnesses and density. This parameterization arises naturally from the way in which the forward Eq. (1) is formulated. However, it is not necessary the most optimal parameterization for seismic inversion. We parameterize our VTI-elastic LWI in terms of relative perturbations of elastic parameters ($\Delta\rho/\rho, \Delta V_{\mathrm{p0}}/V_{\mathrm{p0}}, \Delta V_{\mathrm{s0}}/V_{\mathrm{s0}}, \Delta\epsilon$ and $\Delta\delta$) (Podgornova et al., 2018). We obtain the parameter transformation matrix from chain rule in calculus:

$$\begin{pmatrix}\Delta\rho\\ \Delta C_{11}\\ \Delta C_{13}\\ \Delta C_{33}\\ \Delta C_{55}\end{pmatrix} = \begin{pmatrix} \rho & 0 & 0 & 0 & 0\\ (1+2\epsilon)\rho V_{\mathrm{p0}}^2 & 2(1+2\epsilon)\rho V_{\mathrm{p0}}^2 & 0 & 2\rho V_{\mathrm{p0}}^2 & 0\\ \rho M - \rho V_{\mathrm{s0}}^2 & \dfrac{M_1}{M} & \dfrac{M_2}{M} - 2\rho V_{\mathrm{s0}}^2 & 0 & \dfrac{M_3}{M}\\ \rho V_{\mathrm{p0}}^2 & 2\rho V_{\mathrm{p0}}^2 & 0 & 0 & 0\\ \rho V_{\mathrm{s0}}^2 & 0 & 2\rho V_{\mathrm{s0}}^2 & 0 & 0 \end{pmatrix}\begin{pmatrix}\dfrac{\Delta\rho}{\rho}\\ \dfrac{\Delta V_{\mathrm{p0}}}{V_{\mathrm{p0}}}\\ \dfrac{\Delta V_{\mathrm{s0}}}{V_{\mathrm{s0}}}\\ \Delta\epsilon\\ \Delta\delta\end{pmatrix}, \tag{17}$$

where

$$\begin{aligned} M_1 &= 2\rho(2\delta+1)V_{\mathrm{p0}}^4 - 2\rho(\delta+1)V_{\mathrm{p0}}^2V_{\mathrm{s0}}^2,\\ M_2 &= -2\rho(\delta+1)V_{\mathrm{p0}}^2V_{\mathrm{s0}}^2 + 2\rho V_{\mathrm{s0}}^4,\\ M_3 &= \rho V_{\mathrm{p0}}^4 - \rho V_{\mathrm{p0}}^2V_{\mathrm{s0}}^2,\\ M &= \sqrt{2\delta V_{\mathrm{p0}}^2\left(V_{\mathrm{p0}}^2 - V_{\mathrm{s0}}^2\right) + \left(V_{\mathrm{p0}}^2 - V_{\mathrm{s0}}^2\right)^2}. \end{aligned} \tag{18}$$

The first-order Born approximation is a linear mapping from multi-parameter images to multicomponent seismic data:

$$\Delta\mathbf{d} = \mathscr{L}\Delta\mathbf{m}, \tag{19}$$

where $\mathscr{L}$ is the Born approximation modeling operator ($\mathscr{L} = -\mathscr{R}(\mathscr{A}^0)^{-1}\frac{\partial\mathscr{A}}{\partial\mathbf{m}}\mathbf{u}^0$), $\Delta\mathbf{d}$ is scattered seismic data and $\Delta\mathbf{m}$ is the model vector.

2.2. The linearized inverse problem

The inversion is to find the model vector $\Delta\mathbf{m}$ from the seismic reflection data $\Delta\mathbf{d}$. However, the inverse problem is often ill-posed because of the imperfect sampling of the seismic acquisition geometry. Besides, the observations are usually contaminated with noise that can not be explained by the forward operator. We pose the following linearized waveform inversion for VTI-elastic media:

$$\underset{\Delta\mathbf{m}}{\text{minimize}}\ \chi(\Delta\mathbf{m}) := \| \mathscr{W}_{\mathrm{d}}\left(\mathscr{L}\Delta\mathbf{m} - \Delta\mathbf{d}^{\mathrm{obs}}\right)\|_2^2 + \mu \| \mathscr{W}_{\mathrm{m}}\Delta\mathbf{m}\|_2^2, \tag{20}$$

where $\mathscr{L}$ is the linearized forward modeling operator, $\Delta\mathbf{d}^{\mathrm{obs}}$ represents the multicomponent reflection data, $\Delta\mathbf{m}$ denotes model vector, $\|\bullet\|_2$ represents the L_2 norm of vector, μ is the trade-off parameter, $\mathscr{W}_{\mathrm{d}}$ and $\mathscr{W}_{\mathrm{m}}$ are a priori weighting operators for data and model, respectively. We use the conjugate gradient method (Paige and Saunders, 1982) to solve optimization problem Eq. (20). It is a semi-iterative technique that requires the application of $\mathscr{L}$ and $\mathscr{L}^\dagger$ to vectors in each iteration. The adjoint operator is given by

$$\mathscr{L}^\dagger = -\left(\frac{\partial\mathscr{A}}{\partial\mathbf{m}}\mathbf{u}^0\right)^\dagger\left[\left(\mathscr{A}^0\right)^\dagger\right]^{-1}\mathscr{R}^\dagger, \tag{21}$$

where $\mathscr{R}^\dagger$ is the adjoint of sampling operator that inserts seismic

data at receiver locations and zeros at other locations in the computational domain, $\mathbf{u}^0$ is the source-side incident wavefield, and $(\mathscr{A}^0)^\dagger$ is the adjoint elastic wave operator. The adjoint operator $\mathscr{L}^\dagger$ maps from data space to model image space. The first step in the linearized waveform inversion is functionally similar (but not the same) to pre-stack seismic migration. The detailed derivation of the adjoint operator $\mathscr{L}^\dagger$ is shown in Appendix A.

2.3. Computational cost analysis

In our proposed VTI-elastic LWI, we do not need to explicitly store and invert the Hessian operator ($\mathscr{H} = \mathscr{L}^\dagger\mathscr{L}$). Instead, we apply the conjugate gradient method for solving the linear system of equations. Each iteration requires the application of $\mathscr{L}$ and $\mathscr{L}^\dagger$ on vectors. The forward operator $\mathscr{L}$ needs two forward simulations via finite-difference (FD): one for source-side wavefield and another for Born modeling. The adjoint operator $\mathscr{L}^\dagger$ requires two FD simulations including forward propagation of source-side wavefield and backward propagation of receiver-side wavefield. The application of forward and adjoint operators are repeated for each shot and iteration. The total computational cost of the proposed inversion algorithm is $4N_sN_i$ forward simulations, where N_s is the number of shots and N_i is the number of iterations. Therefore, the order of operations of VTI-elastic LWI is $\mathscr{O}(N_sN_iN_{x_1}N_{x_3}N_tN_o)$, where N_{x_1} and N_{x_3} are the number of grids in x_1 and x_3 directions, N_t is the number of time samples, and N_o is the FD order. The computer program mainly allocates memory for elastic parameter models and time slice of wavefields. Therefore, the memory storage cost of the LWI is proportional to the size of the model $\mathscr{O}(N_{x_1}N_{x_3})$.

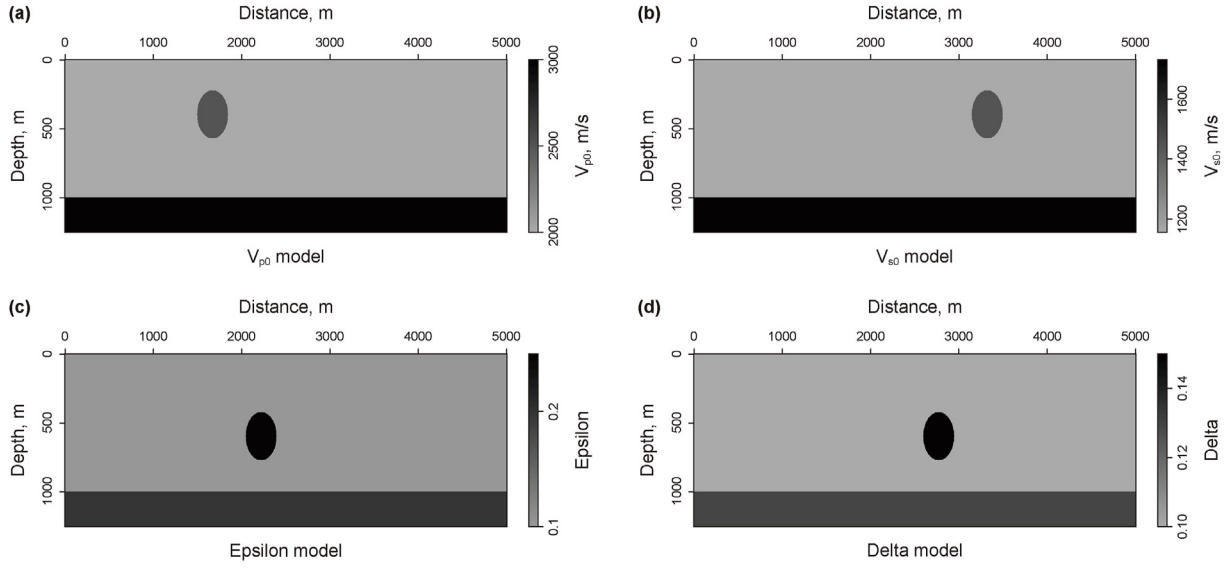

Fig. 1. Layer-inclusion VTI-elastic model. **(a)** Vertical P-wave velocity V_{p0} model. **(b)** Vertical S-wave velocity V_{s0} model. **(c)** Thomsen anisotropy parameter ϵ model. **(d)** Thomsen anisotropy parameter δ model.

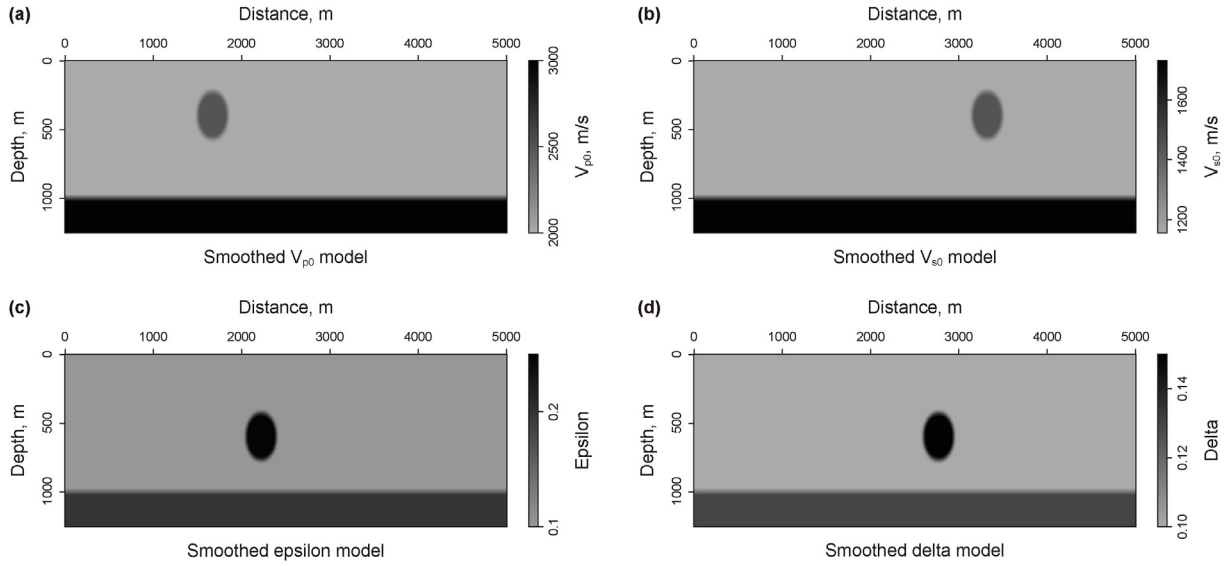

Fig. 2. Smoothed layer-inclusion VTI-elastic model. **(a)** Vertical P-wave velocity V_{p0} model. **(b)** Vertical S-wave velocity V_{s0} model. **(c)** Thomsen anisotropy parameter ϵ model. **(d)** Thomsen anisotropy parameter δ model.

3. Examples

We present a series of numerical examples to illustrate the performance of the proposed VTI-elastic LWI algorithm. The synthetic numerical examples are also used to investigate the resolving power of seismic data for different elastic parameters. For applications in field data, advance data preprocessing such as direct wave muting, surface wave and multiples removal are required to obtain amplitude-preserving primary reflections.

3.1. Layer-inclusion VTI-elastic model example

As a first example, we consider a layer-inclusion VTI-elastic model. This example illustrates the performance of LWI for multi-parameter decoupling. Fig. 1 shows the vertical velocities and Thomsen anisotropy parameters for the layer-inclusion model.

We have assumed that the density is constant at 1500 kg/m^3. The size of the model is 1001 $\times$ 251 grid points with spatial sampling of 5 m. We simulate a synthetic seismic profile with 101 shot locations uniformly distributed along the surface of the model. The geophones are uniformly distributed every 5 m, from $x = 0$ to $x = 5000$ m. The source is a point source modulated in time by a Ricker function with a peak frequency of 20 Hz. Fig. 2 shows the smoothed reference model for inversion and Fig. 3 shows the true velocity and Thomsen parameter perturbations with respect to reference model.

The elastic images obtained by applying the adjoint-based migration operator (first iteration of LWI) to shot gathers are shown in Fig. 4. The images contain remnant low-frequency artifacts after Laplacian filtering (Kang and Cheng, 2012). Moreover, the images contain notable multi-parameter crosstalk, because the different parameter are intrinsically coupled. We can also note that

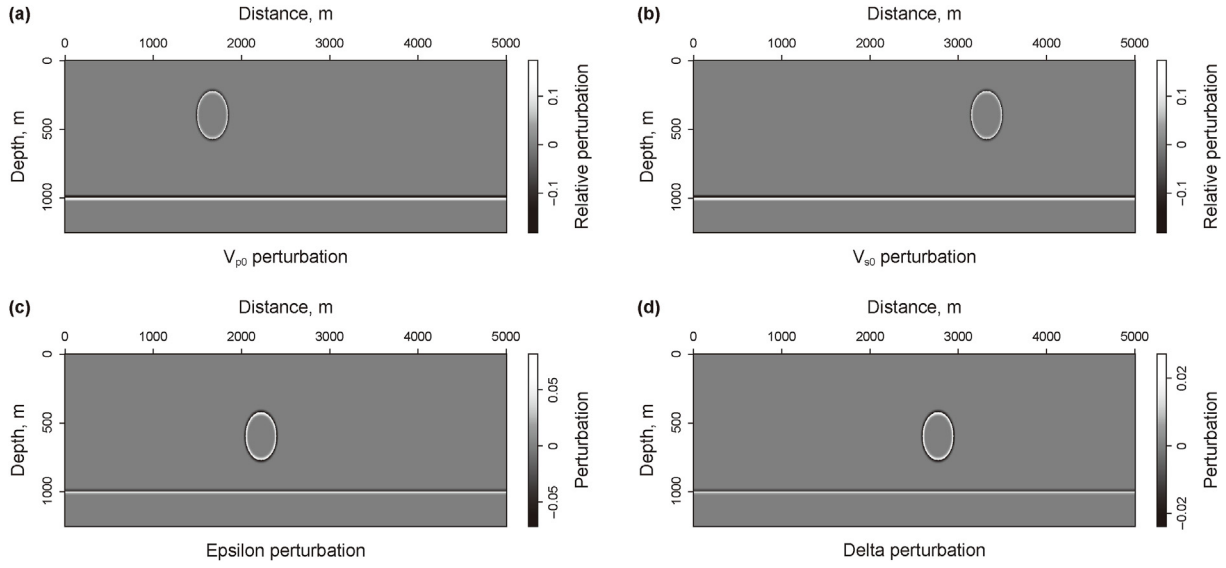

Fig. 3. True model perturbations of layer-inclusion VTI-elastic model. **(a)** Relative perturbation of P-wave vertical velocity $\frac{\Delta V_{p0}}{V_{p0}}$. **(b)** Relative perturbation of S-wave vertical velocity $\frac{\Delta V_{s0}}{V_{s0}}$. **(c)** Perturbation of Thomsen parameter $\Delta\epsilon$. **(d)** Perturbation of Thomsen parameter $\Delta\delta$.

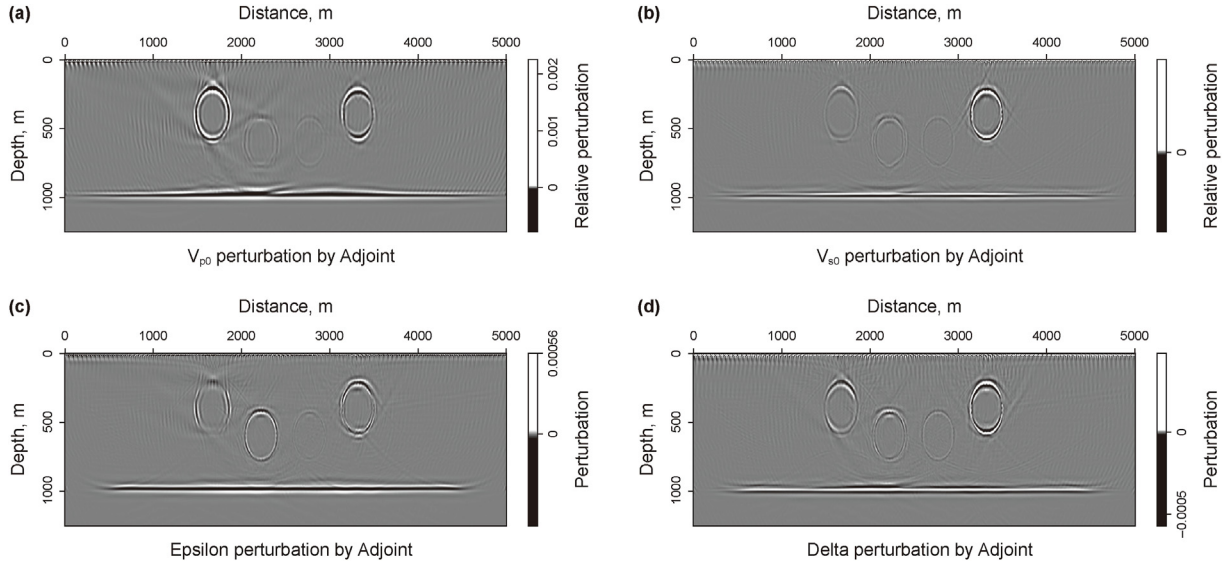

Fig. 4. Model perturbations estimated by adjoint operator (first iteration of LWI). **(a)** Relative perturbation of P-wave vertical velocity $\frac{\Delta V_{p0}}{V_{p0}}$. **(b)** Relative perturbation of S-wave vertical velocity $\frac{\Delta V_{s0}}{V_{s0}}$. **(c)** Perturbation of Thomsen parameter $\Delta\epsilon$. **(d)** Perturbation of Thomsen parameter $\Delta\delta$.

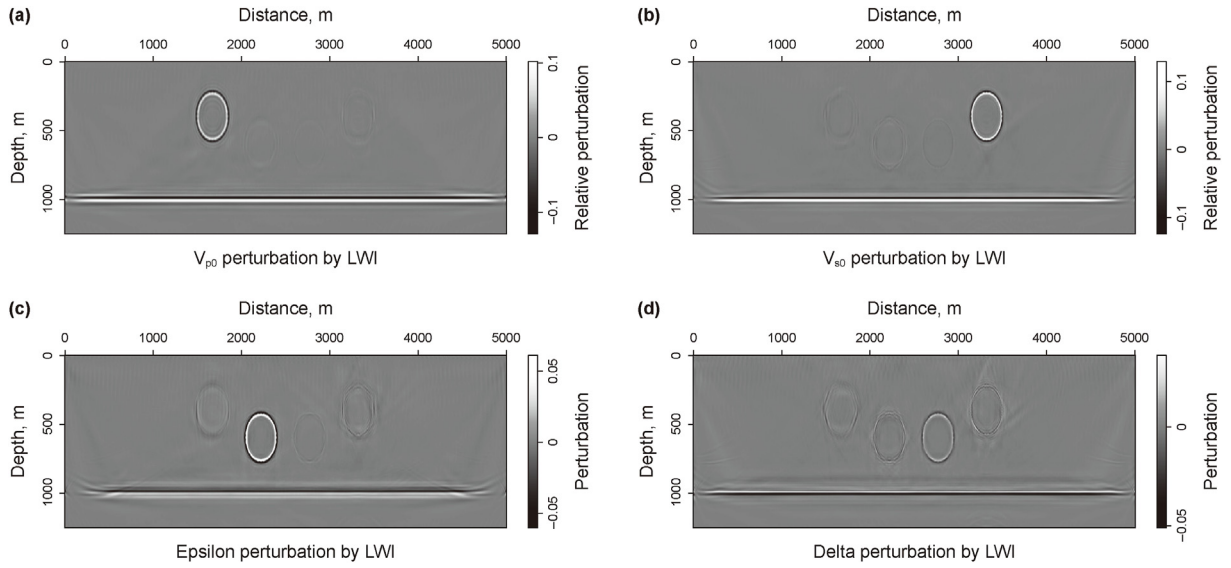

Fig. 5. Model perturbations estimated by proposed VTI-elastic LWI. **(a)** Relative perturbation of P-wave vertical velocity $\frac{\Delta V_{p0}}{V_{p0}}$. **(b)** Relative perturbation of S-wave vertical velocity $\frac{\Delta V_{s0}}{V_{s0}}$. **(c)** Perturbation of Thomsen parameter $\Delta\epsilon$. **(d)** Perturbation of Thomsen parameter $\Delta\hat{\delta}$.

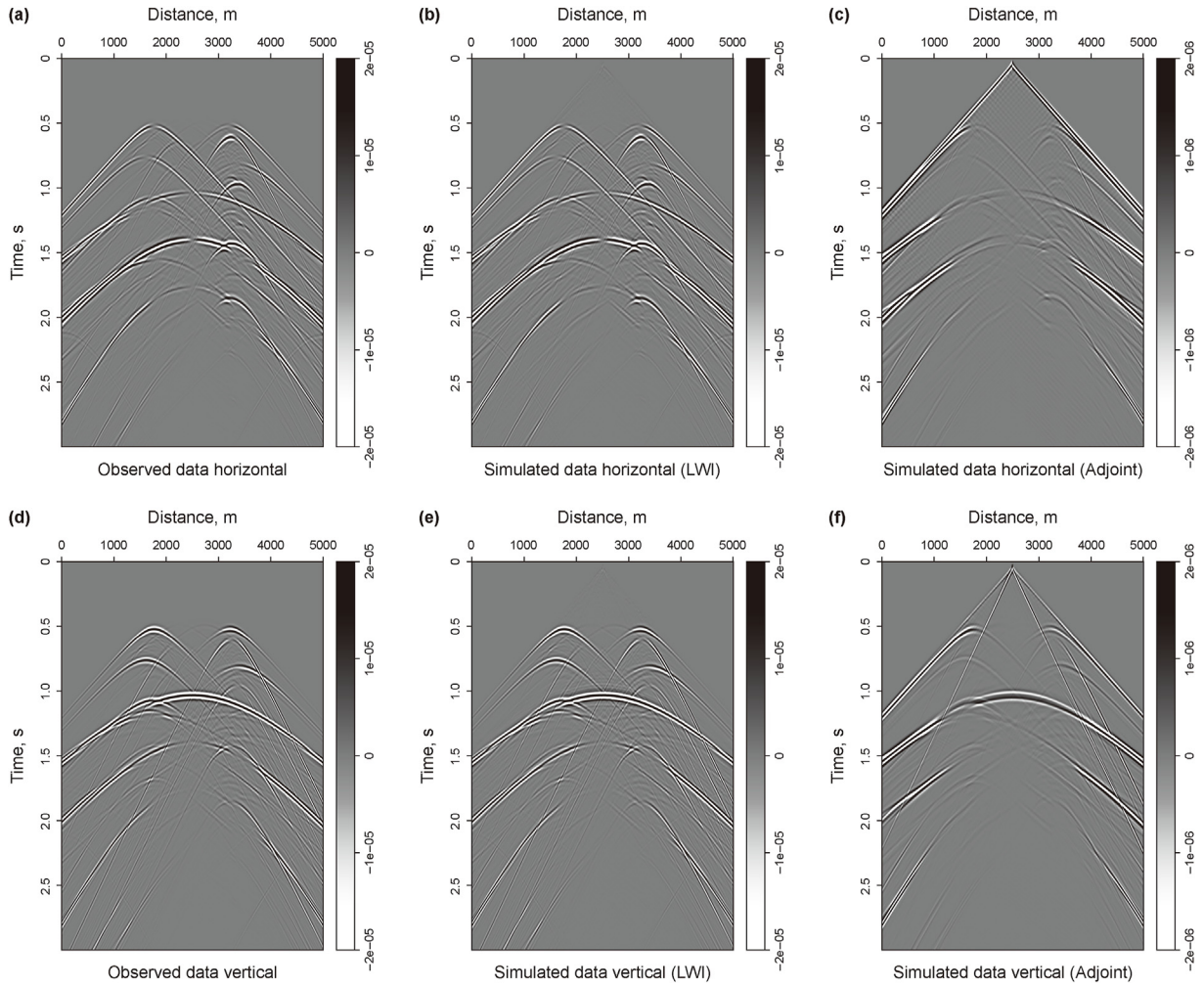

Fig. 6. Data prediction of imaging and inversion results for layer-inclusion VTI-elastic model. **(a)** Observed horizontal component data. **(b)** Predicted horizontal component data by VTI-elastic LWI. **(c)** Predicted horizontal component data by adjoint operator (first iteration of LWI). **(d)** Observed vertical component data. **(e)** Predicted vertical component data by VTI-elastic LWI. **(f)** Predicted vertical component data by adjoint operator (first iteration of LWI).

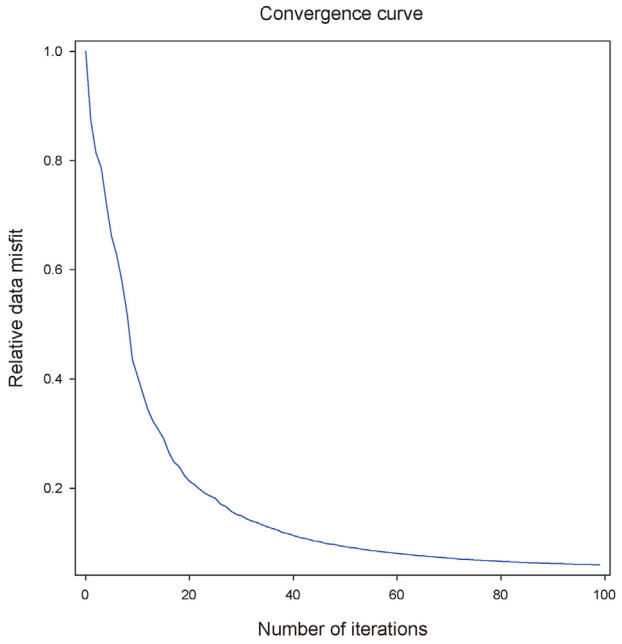

Fig. 7. Convergence curve of VTI-elastic LWI for layer-inclusion VTI-elastic model.

the multi-parameter images have unbalanced amplitude response due to geometric spreading and uneven illumination of the wavefields.

Fig. 5 shows the inversion results obtained by our proposed VTI-elastic LWI. The iterative inversion reduces the low-frequency artifacts and acquisition footprint in the images. Comparing with the adjoint-based images, both vertical and horizontal resolutions are enhanced and the amplitude response is improved by the inversion. More important, the VTI-elastic LWI attenuates the multi-parameter crosstalk through iterative data fitting. The results by linearized waveform inversion are not perfect due to the ill-conditioned nature of the inverse problem. The isotropic parameters (V_{p0} and V_{s0}) are better resolved than the anisotropic parameters (ϵ and δ). The Thomsen anisotropy parameters are more prone to multi-parameter coupling. Especially, the parameter δ is the most difficult parameter to recover. The reason for this phenomenon is that Thomsen parameter δ has less impact on the reflection seismic data comparing with other elastic parameters (Podgornova et al., 2018). We analyze the multi-parameter crosstalk using ray-Born approximation in Appendix B. We plot the radiation patterns of VTI-elastic scatters for P–P, P–S, S–P, and S–S wave in Fig. 19. The radiation pattern of δ resembles the parameter ϵ and has smaller scattering response.

In Fig. 6, we evaluate the data fitting property of adjoint-based migration and linearized waveform inversion. It confirms that the data fitting by inversion-based images is much better than that of adjoint-based images. Finally, Fig. 7 shows the normalized cost function versus iteration number for the proposed VTI-elastic LWI method. The latter demonstrates that the proposed VTI-elastic LWI algorithm converges properly.

3.2. Hess VTI-elastic model example

For a more complicated example, we next consider a modified version of the VTI-elastic Hess model. We design the VTI-elastic Hess model based on the original VTI-acoustic version (Fig. 8). This model contains a salt structure with high-velocity contrasts that challenges the seismic imaging and inversion algorithms. Note that the anisotropy parameters are uncorrelated with the velocities in the region near horizontal distance of 5000 m and depth 1500 m. The model grid increments are $dx = dz = 10$ m. There are 181 shots and 901 receivers evenly distributed on the surface of the earth. The source function used to excite the wavefield is a 15 Hz peak frequency Ricker wavelet. Figs. 9 and 10 show the reference model and the true model perturbation with respect to the reference model, respectively.

Fig. 11 presents the elastic images estimated by adjoint-based migration operator (first iteration of LWI). Despite Laplacian filtering, the adjoint-based images contain strong low frequency artifacts overwhelming the shallow layers. Because of geometric

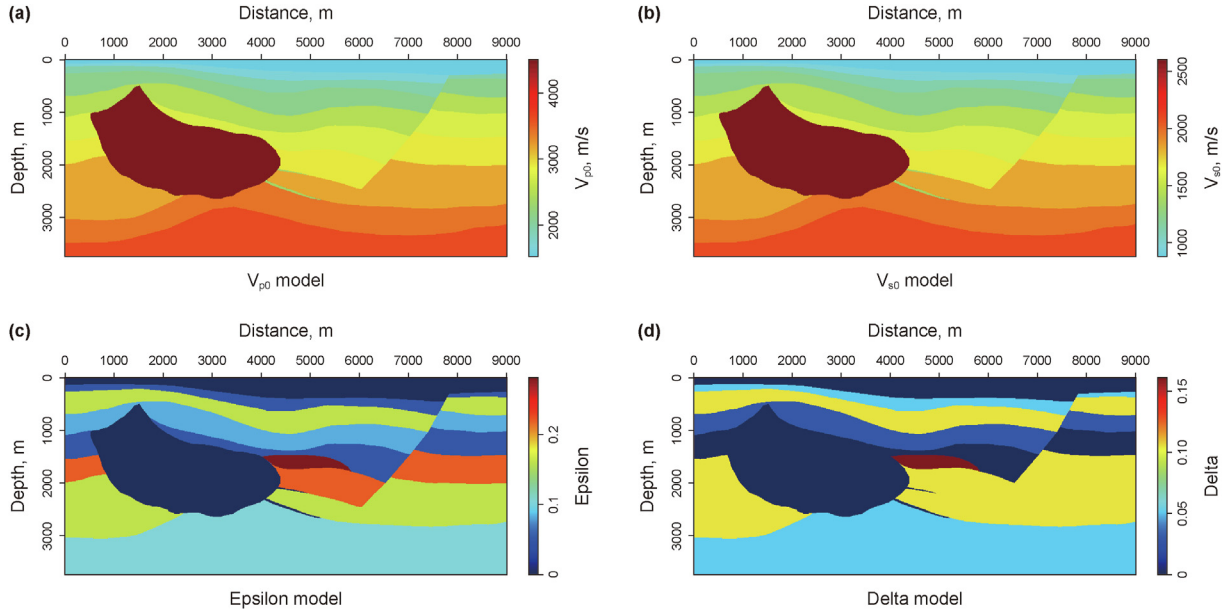

Fig. 8. Hess VTI-elastic model. **(a)** Vertical P-wave velocity V_{p0} model. **(b)** Vertical S-wave velocity V_{s0} model. **(c)** Thomsen anisotropy parameter ϵ model. **(d)** Thomsen anisotropy parameter δ model.

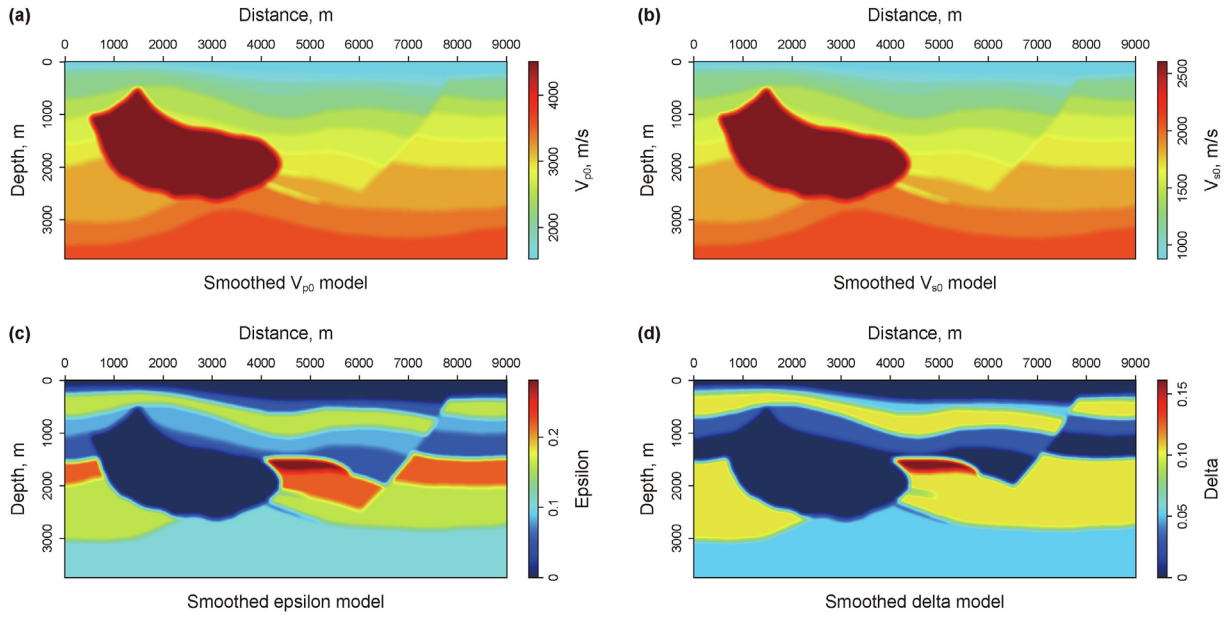

Fig. 9. Smoothed Hess VTI-elastic model. **(a)** Vertical P-wave velocity V_{p0} model. **(b)** Vertical S-wave velocity V_{s0} model. **(c)** Thomsen anisotropy parameter ϵ model. **(d)** Thomsen anisotropy parameter δ model.

spreading effects, the image amplitude is weaker in the deep part than in the shallow part. The adjoint-based images do not reveal accurate quantitative information about the heterogeneity. The results of inversion-based VTI-elastic LWI are shown in Fig. 12. Compared with adjoint-based images, the inversion improves the horizontal and vertical spatial resolution throughout the images. It also corrects the geometric spreading effects that boosting up the image amplitude in the deeper part. Besides, the linearized inversion remarkably attenuates low-frequency artifacts in images via iterative data fitting.

Fig. 13 shows the data prediction of results obtained by adjoint operator and results from inversion-based VTI-elastic LWI. The data predicted by VTI-elastic LWI results are much better than the ones by adjoint operator. The normalized data misfit curve in Fig. 14 also demonstrates that the inverted elastic images fit the observed data.

3.3. The influence of observation noise

We add noise to the data to test the robustness of the proposed VTI-elastic LWI to observation noise. Noise is simulated using random numbers drawing from a normal distribution. Then, we filter the noise trace to the same frequency range of the clean signal. Last, we scale the noise trace to a signal-to-noise ratio (SNR) and add it to the clean signal. In our study, the SNR is defined as follows:

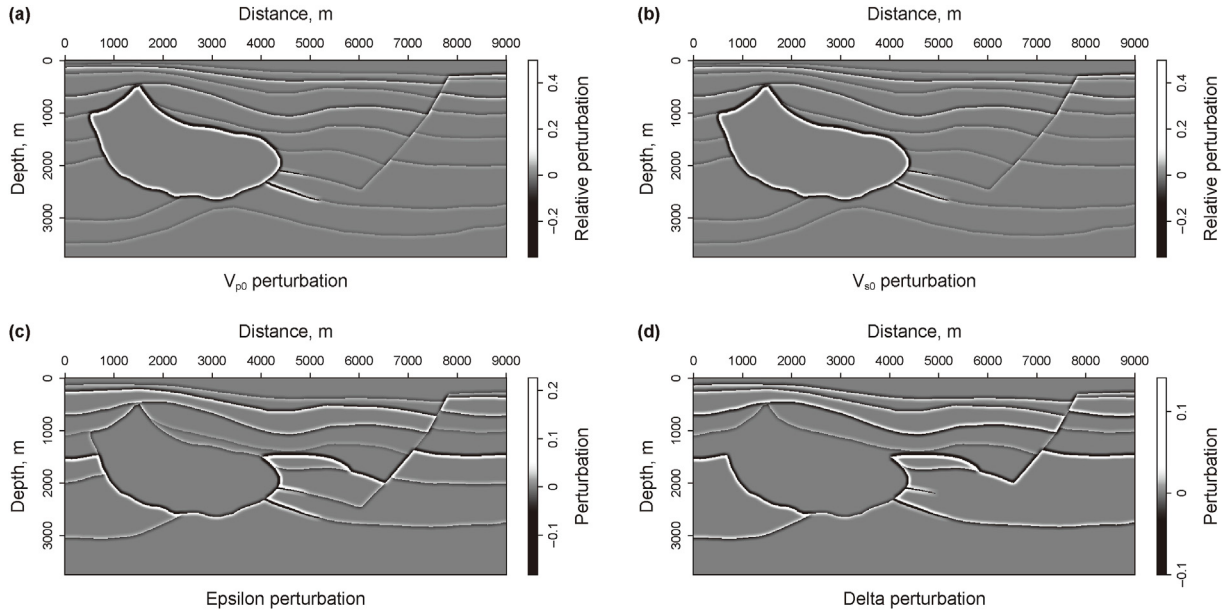

Fig. 10. True model perturbations of Hess VTI-elastic model. **(a)** Relative perturbation of P-wave vertical velocity $\frac{\Delta V_{p0}}{V_{p0}}$. **(b)** Relative perturbation of S-wave vertical velocity $\frac{\Delta V_{s0}}{V_{s0}}$. **(c)** Perturbation of Thomsen parameter $\Delta\epsilon$. **(d)** Perturbation of Thomsen parameter $\Delta\delta$.

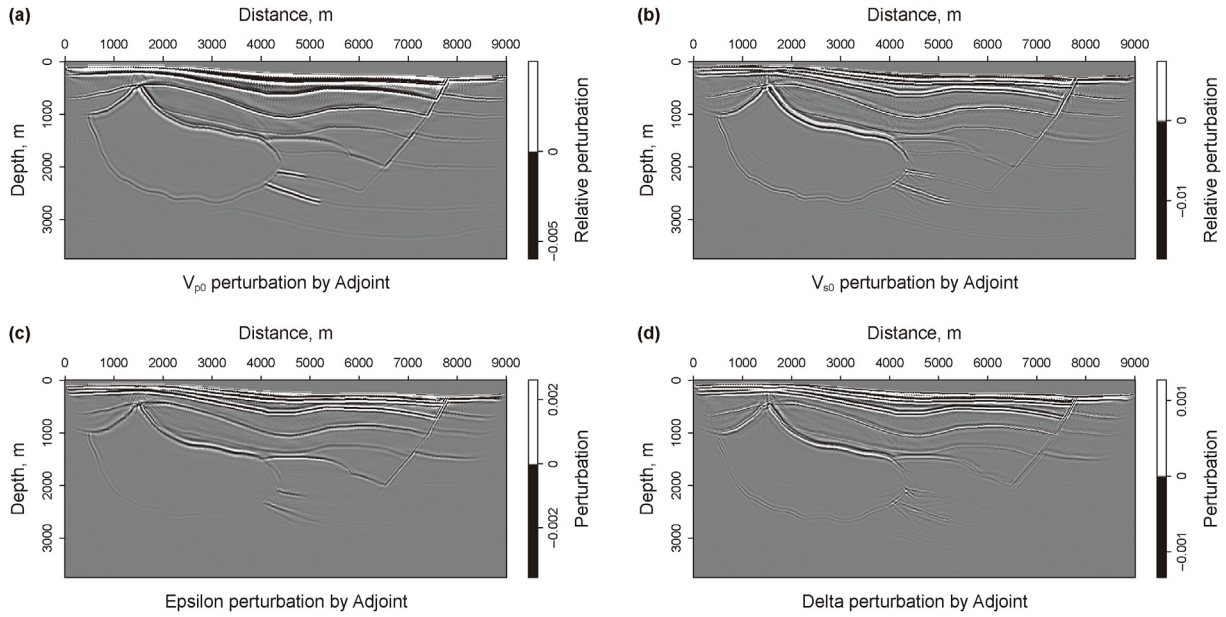

Fig. 11. Model perturbations estimated by adjoint operator (first iteration of LWI). **(a)** Relative perturbation of P-wave vertical velocity $\frac{\Delta V_{p0}}{V_{p0}}$. **(b)** Relative perturbation of S-wave vertical velocity $\frac{\Delta V_{s0}}{V_{s0}}$. **(c)** Perturbation of Thomsen parameter $\Delta\epsilon$. **(d)** Perturbation of Thomsen parameter $\Delta\delta$.

$$\mathrm{SNR} = 10\log_{10}\left(\frac{A_s}{A_n}\right)^2. \tag{22}$$

here, A_s and A_n are the root-mean-square (RMS) values of seismic signal and noise, respectively. Fig. 15 displays one of the noisy data gathers under different noise conditions. We perform the proposed LWI on this noisy dataset. As expected, the presence of data noise deteriorates the estimated model perturbations as shown in Fig. 16. The inversion results of velocity perturbations from noisy data are roughly similar with the ones from noise-free data. The results of Thomsen anisotropy parameters are more prone to observation noise in data. There are noise artifacts in the recovered results for Thomsen anisotropy parameter perturbations. However, the main features of the inverted model are still valid.

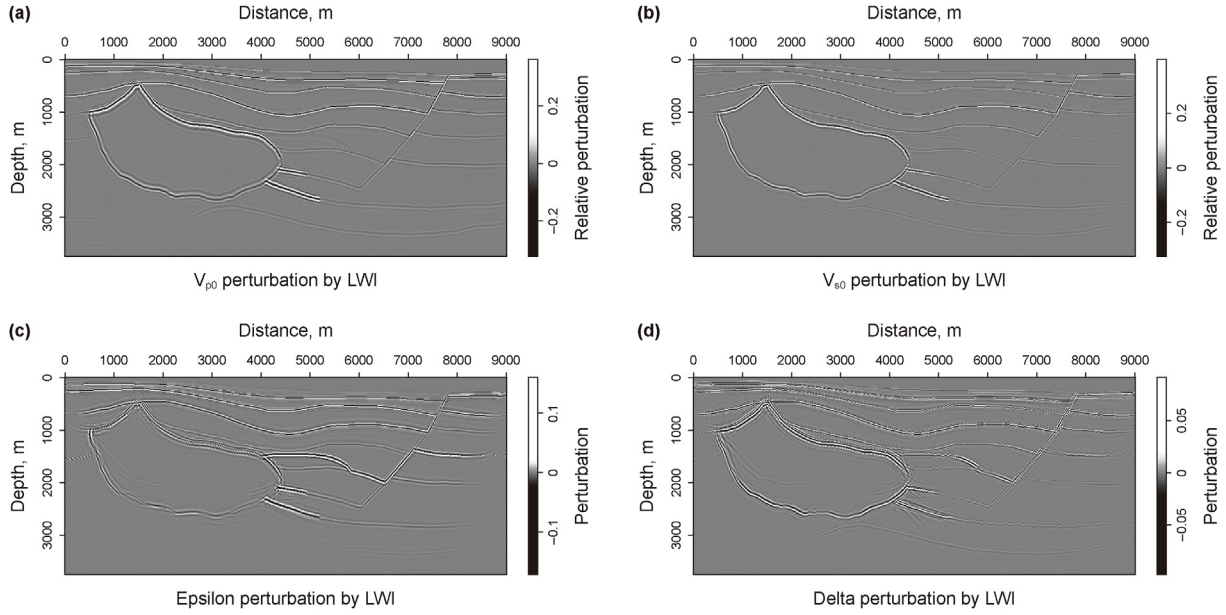

Fig. 12. Model perturbations estimated by proposed VTI-elastic LWI. **(a)** Relative perturbation of P-wave vertical velocity $\frac{\Delta V_{p0}}{V_{p0}}$. **(b)** Relative perturbation of S-wave vertical velocity $\frac{\Delta V_{s0}}{V_{s0}}$. **(c)** Perturbation of Thomsen parameter $\Delta\epsilon$. **(d)** Perturbation of Thomsen parameter $\Delta\delta$.

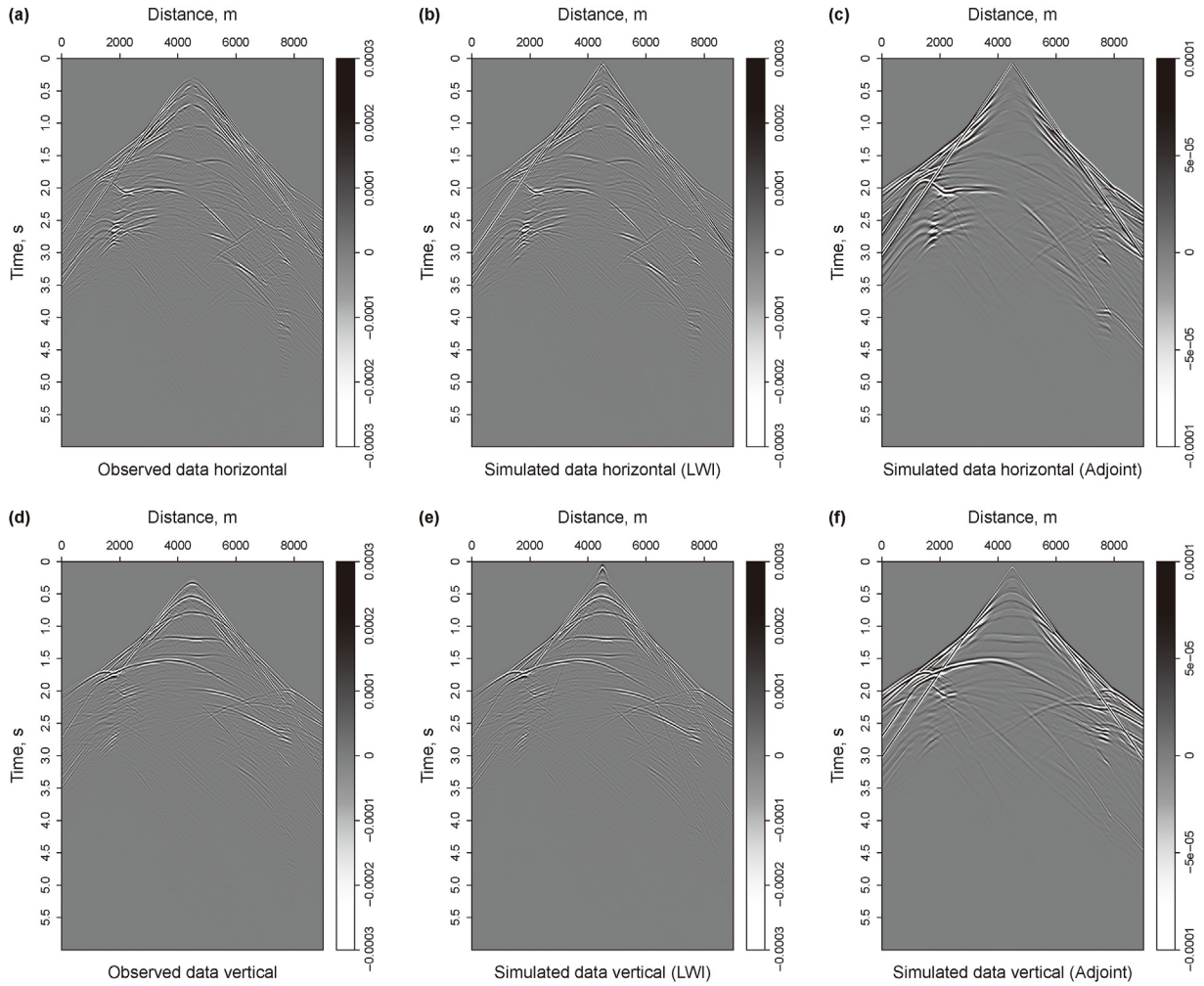

Fig. 13. Data prediction of imaging and inversion results for Hess VTI-elastic model. **(a)** Observed horizontal component data. **(b)** Predicted horizontal component data by VTI-elastic LWI. **(c)** Predicted horizontal component data by adjoint operator (first iteration of LWI). **(d)** Observed vertical component data. **(e)** Predicted vertical component data by VTI-elastic LWI. **(f)** Predicted vertical component data by adjoint operator (first iteration of LWI).

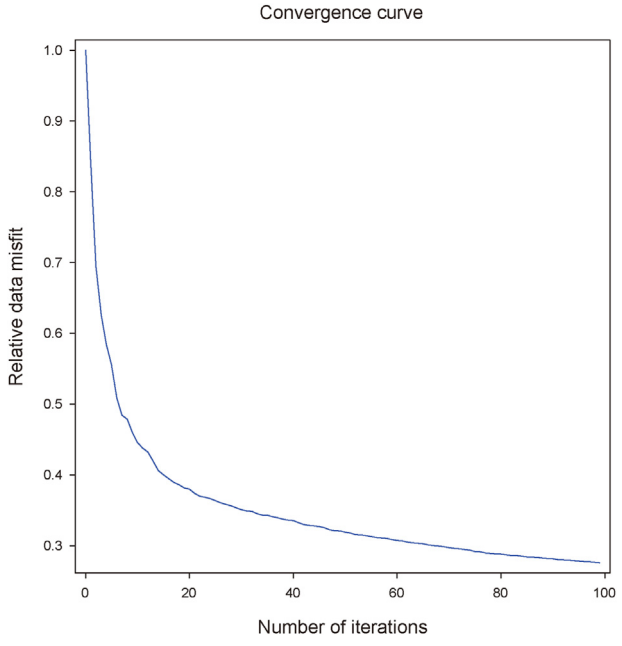

Fig. 14. Convergence curve of VTI-elastic LWI for Hess VTI-elastic model.

3.4. The influence of reference model error

The error in reference model will influence inversion results. In this section, we test the sensitivity of the VTI-elastic LWI to inaccuracy of the reference model (vertical velocities and anisotropic parameters). We heavily smooth the reference model using 2D Gaussian functions of width 100 × 100 m (20 × 20 grids) and 150 × 150 m (30 × 30 grids). Fig. 17 shows the smoothed reference model and true model perturbations for vertical velocities and Thomsen parameters. The other setup of the numerical example is the same with the one used in Fig. 5. Fig. 18 shows the inversion results using the reference model with different degree of smoothing. With larger model error, the inversion results of VTI-elastic LWI show less quality with more uncollapsed artifacts. More importantly, inversion results show more multi-parameter crosstalk artifacts when reference model is less accurate. Similarly, we observe that Thomsen anisotropic parameters are more seriously deteriorated by the model error.

4. Discussion

The seismic imaging entails inferring the spatial locations of rapid variations of subsurface mechanical properties (reflectivity

function). Whereas, the seismic inversion is to quantitatively estimate the size of changes in subsurface mechanical properties (Stolt and Weglein, 2012). In exploration seismology, the term "least-squares migration" has been used interchangeably to refer to "imaging" or "inversion" for a long time. In constant-density acoustic case, the PP reflectivity is a function of P-wave velocity perturbation and opening angle between incident and reflected waves. However, in elastic case, there exists multi-component images (e.g. PP, PS, SP, SS) and multi-parameter model perturbations (e.g. $\Delta\rho$, ΔC_{ij}). The difference between "imaging" and "inversion" is more remarkable. In "elastic least-squares imaging", the PP, PS, SP, SS images are retrieved from reflection seismic data. The PP, PS, SP, SS images can be stacked images or angle-domain image volumes. In "elastic linearized waveform inversion", the elastic model parameter perturbations are inverted from the seismic data that reveal the intrinsic rock properties. In this article, we develop a VTI-elastic linearized waveform inversion method that simultaneously inverts for the vertical velocity perturbations and Thomsen parameter perturbations ($\Delta V_{p0}/V_{p0}$, $\Delta V_{s0}/V_{s0}$, $\Delta\epsilon$ and $\Delta\delta$). The method falls in the scope of "inversion" that quantitatively estimates localized model perturbations from the long wave-length reference model of subsurface mechanical properties. Besides, the inverted subsurface properties can also serve as images for seismic interpretation to help locate hydrocarbon reservoirs. We have compared the images obtained by adjoint operator and inversion-based VTI-elastic LWI. We have observed that the multi-parameter crosstalk issue in Thomsen parameters is more prominent than in velocities. The Thomsen parameter δ is the most difficult to resolve. Liu et al. (2019) made a similar observation in the frequency-domain Gauss-Newton VTI-elastic full-waveform

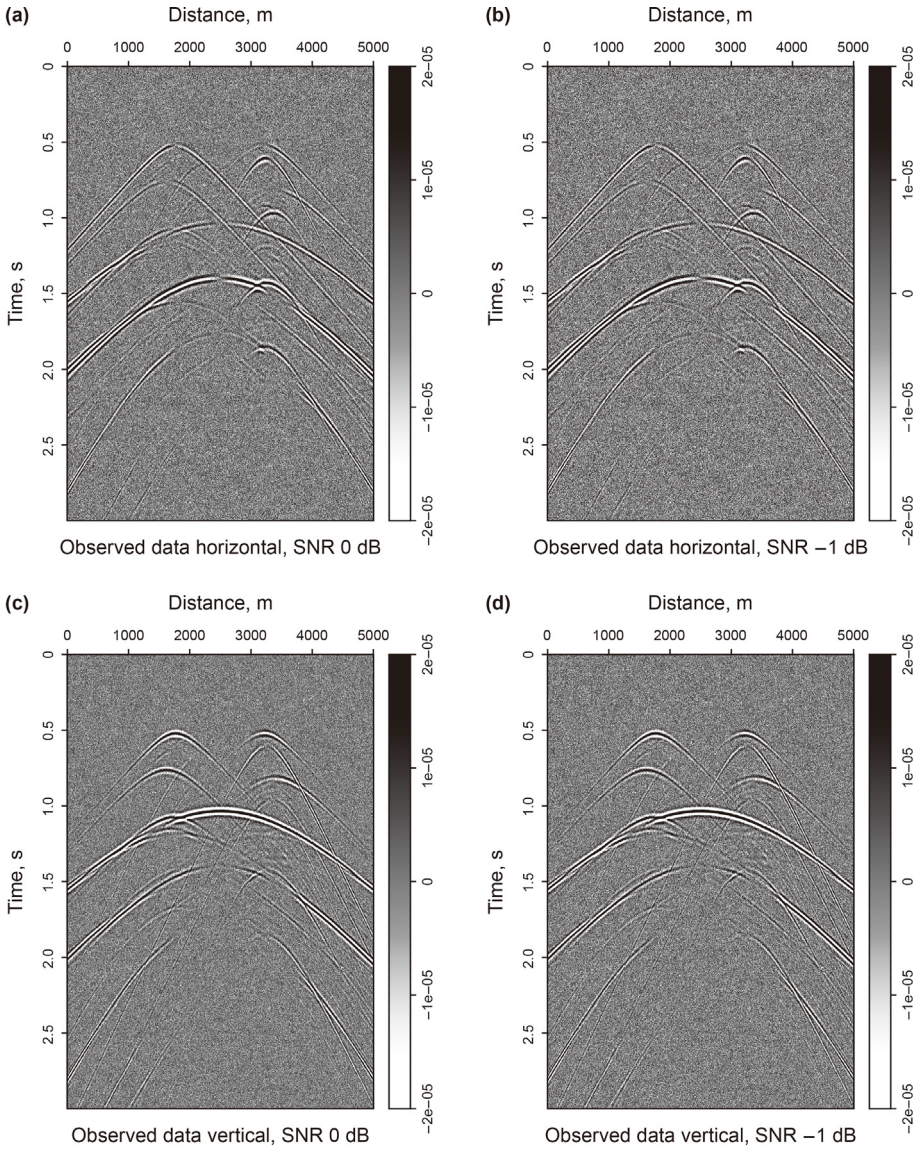

Fig. 15. Noisy data with different SNRs for layer-inclusion VTI-elastic model. **(a)** Horizontal component noisy data (SNR = 0 dB). **(b)** Horizontal component noisy data (SNR = −1 dB). **(c)** Vertical component noisy data (SNR = 0 dB). **(d)** Vertical component noisy data (SNR = −1 dB).

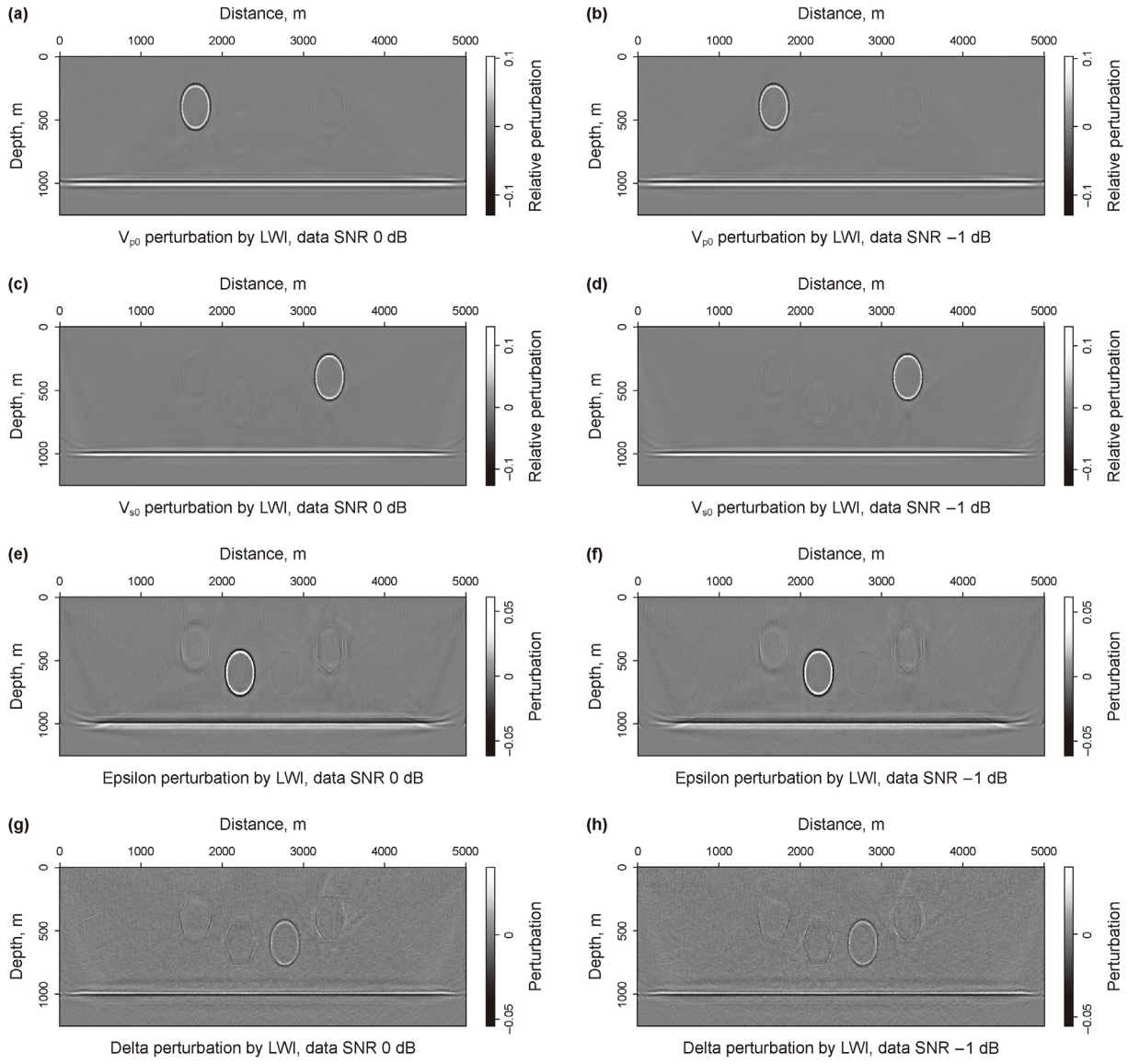

Fig. 16. Model perturbations estimated by proposed VTI-elastic LWI using noisy data. Estimated $\frac{\Delta V_{p0}}{V_{p0}}$ using noisy data with SNR 0 dB **(a)** and noisy data with SNR −1 dB **(b)**. Estimated $\frac{\Delta V_{s0}}{V_{s0}}$ using noisy data with SNR 0 dB **(c)** and noisy data with SNR −1 dB **(d)**. Estimated $\Delta\epsilon$ using noisy data with SNR 0 dB **(e)** and data with SNR −1 dB **(f)**. Estimated $\Delta\delta$ using noisy data with SNR 0 dB **(g)** and data with SNR −1 dB **(h)**.

inversion experiments. Note that, the VTI-elastic FWI by Liu et al. (2019) is a frequency-domain approach. It is based on the improved scattering-integral method that needs to explicitly compute the wavefields for each source and the Green's function for each receiver, and then store them in computer memory. Our VTI-elastic linearized waveform inversion is a time domain approach and is based on adjoint-state method that applies forward and adjoint operators "on the fly" to vectors. Podgornova et al. (2018) analyzed the resolution limits of weakly VTI elastic multi-parameter inversion based on singular value decomposition (SVD) of analytical Fréchet derivative (sensitivity) matrix. They observed that PP scattering wave resolves no more than three elastic parameters and PS scattering waves resolves no more than four elastic parameters. In the latter case, the fourth parameter is less resolvable and has narrower sensitive wavenumber band. We have analyzed the multi-parameter crosstalk in linearized waveform inversion for VTI-elastic media based on the analytical formulas for the radiation patterns derived in Appendix B. The radiation patterns are derived using the Born approximation and high-frequency, far-field asymptotic Green's function (or called ray-Born approximation). The radiation patterns for P–P, P–S, S–P, and S–S wave are plotted as Fig. 19. Optimal parameterization for VTI anisotropic elastic multi-parameter full-waveform inversion is complicated and still an open question for further investigation (Kamath and Tsvankin, 2016; Pan et al., 2016, 2020; Kamath et al., 2017; Guitton and Alkhalifah, 2017; He et al., 2018).

Successful application of the proposed method to real seismic data has some prerequisite conditions. First, one needs the access to relatively accurate background reference model for vertical P- and S-wave velocities and Thomsen anisotropic parameters. This can be

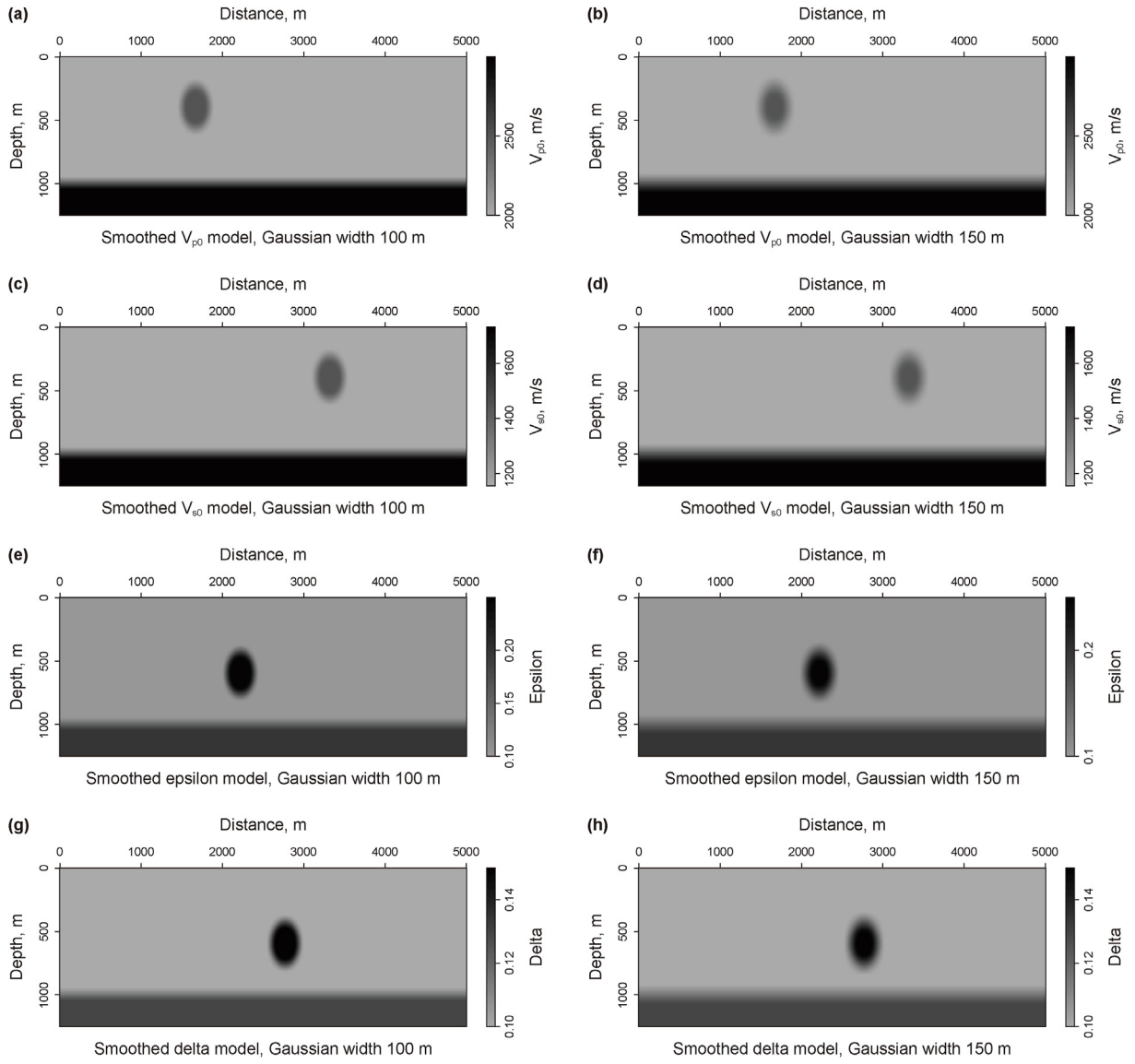

Fig. 17. Layer-inclusion VTI-elastic model with different degree of smoothing. Smoothed vertical P-wave velocity V_{p0} model with Gaussian function of width $W = 100$ m **(a)** and $W = 150$ m **(b)**. Smoothed vertical S-wave velocity V_{s0} model with Gaussian function of width $W = 100$ m **(c)** and $W = 150$ m **(d)**. Smoothed Thomsen anisotropy parameter ϵ model with Gaussian function of width $W = 100$ m **(e)** and $W = 150$ m **(f)**. Smoothed Thomsen anisotropy parameter δ model with Gaussian function of width $W = 100$ m **(g)** and $W = 150$ m **(h)**.

achieved through well-logging and travel-time tomography techniques. Second, the LWI requires relatively high-quality of seismic data. Advance data preprocessing techniques are needed to attenuate seismic noise, remove direct wave and multiples from the seismic data.

5. Conclusion

We study a linearized waveform inversion method for VTI-elastic media and analyze the multi-parameter crosstalk utilizing scattering radiation patterns. The proposed scheme simultaneously inverts for the localized model perturbations $(\Delta V_{p0}/V_{p0}, \Delta V_{s0}/V_{s0}, \Delta\epsilon$ and $\Delta\delta)$ with a prior knowledge of the long-wavelength reference model. Our proposed scheme is an iterative algorithm that requires a forward and an adjoint operator acting on vectors in each iteration. We derive the forward Born modeling operator by perturbation theory and adjoint operator via adjoint-state method. The linearized inversion improves the spatial resolution, reduces image artifacts and multi-parameter crosstalk and improves amplitude response of the elastic images comparing with the adjoint-based images. We have observed that the multi-parameter crosstalk problem is more prominent in the inversion images for Thomsen anisotropy parameters. Especially, the Thomsen parameter δ is the most difficult to resolve. We also analyze the multi-parameter crosstalk using scattering radiation patterns. Moreover, we draw connections and classify differences between least-squares migration and linearized waveform inversion that are often overlooked in seismic imaging/inversion community. The linearized waveform inversion for VTI-elastic media presented in this article provides quantitative information of the rock properties that may help identify oil and gas sweet spot. The high-resolution imaging technique for anisotropic elastic media developed in this article is potentially useful for exploration and exploitation of complex oil and gas reservoirs.

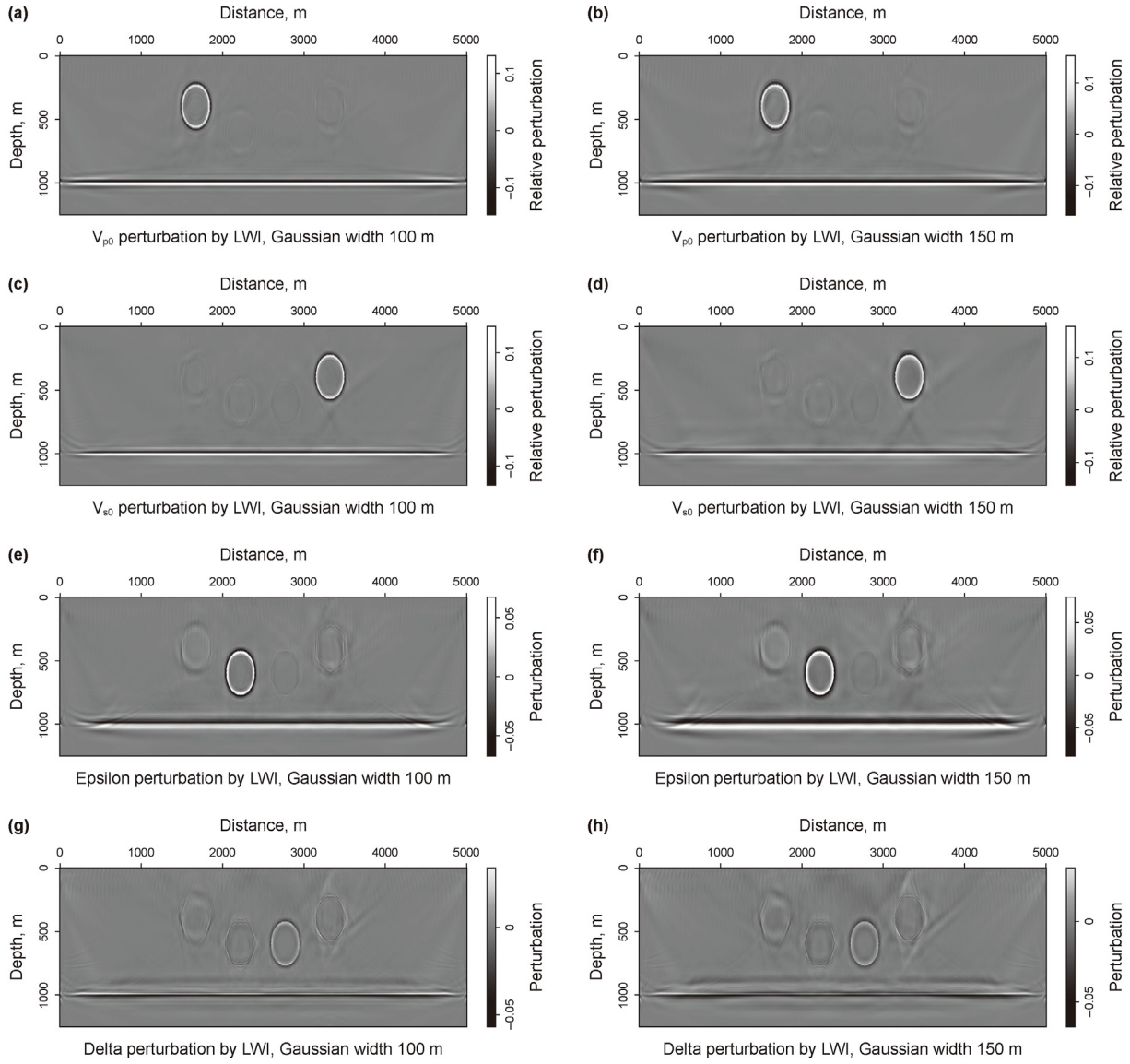

Fig. 18. Results of VTI-elastic LWI with different degree of reference model error. Estimated P-wave velocity relative perturbation $\frac{\Delta V_{p0}}{V_{p0}}$ **(a)**, S-wave velocity relative perturbation $\frac{\Delta V_{s0}}{V_{s0}}$ **(c)**, Thomsen parameter perturbation $\Delta\epsilon$ **(e)** and Thomsen parameter perturbation $\Delta\delta$ **(g)** using reference model smoothed with Gaussian function of width $W = 100$ m. Estimated P-wave velocity relative perturbation $\frac{\Delta V_{p0}}{V_{p0}}$ **(b)**, S-wave velocity relative perturbation $\frac{\Delta V_{s0}}{V_{s0}}$ **(d)**, Thomsen parameter perturbation $\Delta\epsilon$ **(f)** and Thomsen parameter perturbation $\Delta\delta$ **(h)** using reference model smoothed with Gaussian function of width $W = 150$ m.

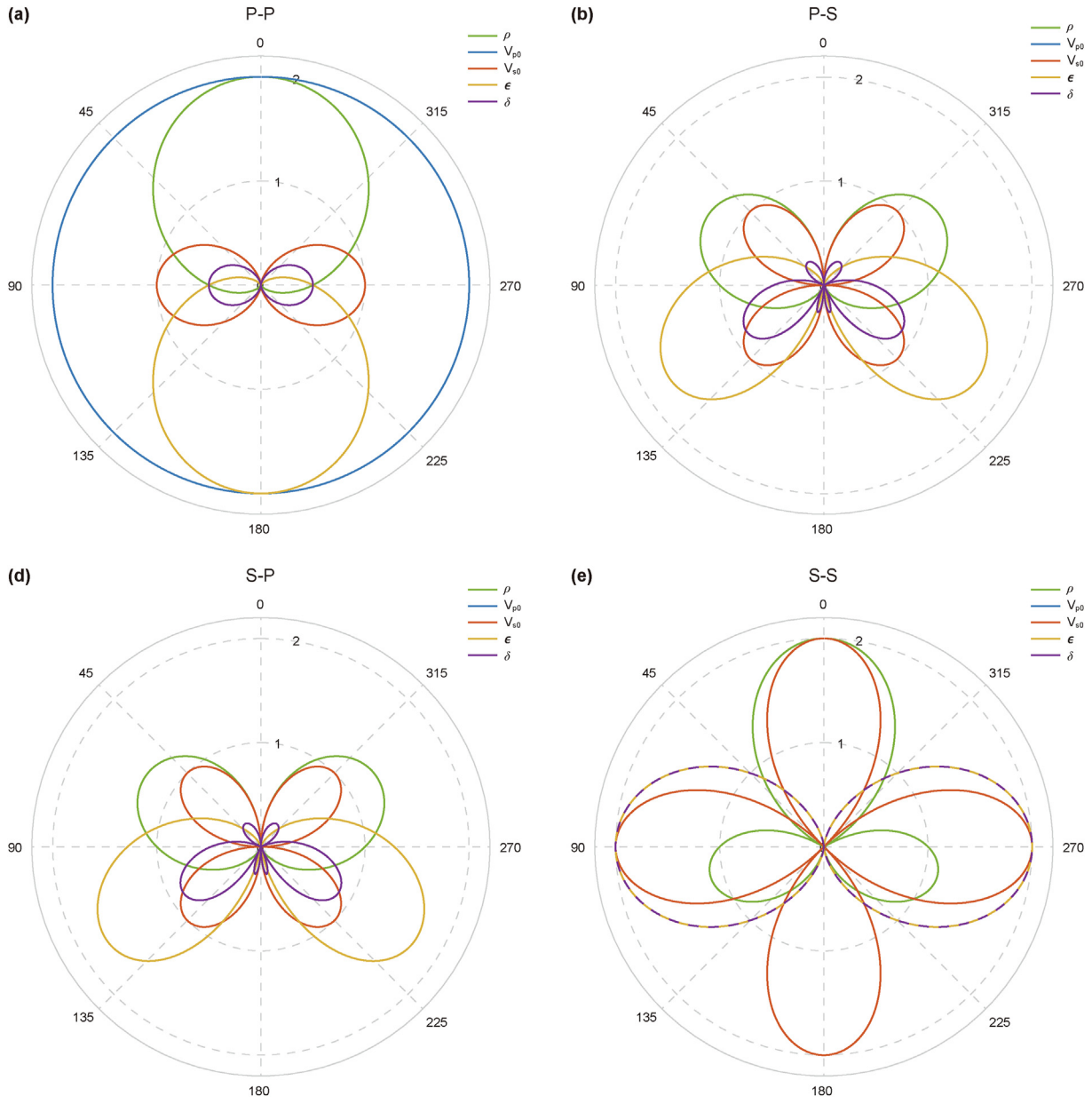

Fig. 19. Radiation patterns for VTI-elastic scatters. **(a)** P–P radiation patterns, **(b)** P–S radiation patterns, **(c)** S–P radiation patterns, **(d)** S–S radiation patterns.

Declaration of competing interest

The authors declare that they have no known competing financial interests or personal relationships that could have appeared to influence the work reported in this paper.

Acknowledgments

We thank anonymous reviewers for their valuable suggestions and comments that improved the manuscript. This study is jointly supported by the National Natural Science Foundation of China (42304132), the National Key R&D Program of China (2021YFA0716803) and the Science Foundation of the China University of Petroleum, Beijing (No. 2462021BJRC006). Figures in this paper were plotted using the Madagascar open-source software package.

Appendix A

Derivation of the adjoint operator

The adjoint operator ($\mathscr{L}^{\dagger}$) of Born approximation modeling operator is derived as follows. The forward Born approximation and adjoint operators satisfy the following inner product condition:

$$\langle \mathbf{\Delta d}, \mathscr{L}\mathbf{\Delta m}\rangle_{\mathbb{D}} = \langle \mathbf{\Delta m}, \mathscr{L}^{\dagger}\mathbf{\Delta d}\rangle_{\mathbb{M}}. \tag{A-1}$$

In the above equation, symbol † represents taking the adjoint of

an operator and $\langle \bullet, \bullet \rangle$ means the inner product in data domain ($\mathbb{D}$) or model domain ($\mathbb{M}$). The adjoint operator is given by

$$\begin{aligned}\Delta\mathbf{m}^* &= \mathscr{L}^\dagger \Delta\mathbf{d} = -\left(\frac{\partial \mathscr{A}}{\partial \mathbf{m}}\mathbf{u}^0\right)^\dagger \left[\left(\mathscr{A}^0\right)^{-1}\right]^\dagger \mathscr{R}^\dagger \Delta\mathbf{d} \\ &= -\left(\frac{\partial \mathscr{A}}{\partial \mathbf{m}}\mathbf{u}^0\right)^\dagger \left[\left(\mathscr{A}^0\right)^\dagger\right]^{-1} \mathscr{R}^\dagger \Delta\mathbf{d}. \end{aligned} \tag{A-2}$$

The adjoint operator in LWI resembles the RTM algorithm for reflection seismic data. We introduce an auxiliary adjoint-state variable $\boldsymbol{\lambda} = [(\mathscr{A}^0)^\dagger]^{-1}\mathscr{R}^\dagger\Delta\mathbf{d}$ to simplify Eq. (A-2):

$$\Delta\mathbf{m}^* = -\left(\frac{\partial \mathscr{A}}{\partial \mathbf{m}}\mathbf{u}^0\right)^\dagger \boldsymbol{\lambda}. \tag{A-3}$$

The above equation means that the adjoint process entails zeros-lag cross-correlation of the source-side wavefield and auxiliary wavefield. The auxiliary wavefield $\boldsymbol{\lambda}$ is the solution of the adjoint formulation of the anisotropic elastic wave equation (Eq. (9)):

$$\left(\mathscr{A}^0\right)^\dagger \boldsymbol{\lambda} = \mathscr{R}^\dagger \Delta\mathbf{d}, \tag{A-4}$$

with

$$\left(\mathscr{A}^0\right)^\dagger = \begin{pmatrix} \rho^0\mathbf{I} & 0 \\ 0 & \mathbf{I} \end{pmatrix}^\dagger \left(\frac{\partial}{\partial t}\right)^\dagger - \begin{pmatrix} 0 & \mathbf{D} \\ \mathbf{C}^0\mathbf{D}^{\mathrm{T}} & 0 \end{pmatrix}^\dagger, \boldsymbol{\lambda} = \begin{pmatrix} \boldsymbol{\varphi} \\ \boldsymbol{\tau} \end{pmatrix}. \tag{A-5}$$

Symbol $(\mathscr{A}^0)^\dagger$ denotes the adjoint elastic wave operator, $\boldsymbol{\varphi}$ and $\boldsymbol{\tau}$ are adjoint particle velocity field and stress field, respectively, and $\mathscr{R}^\dagger\Delta\mathbf{d}$ is the adjoint source. Reformulating Eq. (A-4), one can have the following result:

$$\begin{cases} -\rho^0 \dfrac{\partial \boldsymbol{\varphi}}{\partial t} + \mathbf{D}\left(\mathbf{C}^0\right)^{\mathrm{T}} \boldsymbol{\tau} = \mathscr{R}^\dagger \Delta\mathbf{d}_{\mathrm{v}}, \\ -\dfrac{\partial \boldsymbol{\tau}}{\partial t} + \mathbf{D}^{\mathrm{T}} \boldsymbol{\varphi} = \mathscr{R}^\dagger \Delta\mathbf{d}_{\mathrm{p}}, \end{cases} \tag{A-6}$$

where $\Delta\mathbf{d}_{\mathrm{v}}$ and $\Delta\mathbf{d}_{\mathrm{p}}$ denote the multicomponent particle velocity data and pressure data, respectively. The first-order particle velocity-stress wave equation system is not strictly self-adjoint. We apply a transformation of variables to reformulate the adjoint equation system:

$$\tilde{\boldsymbol{\varphi}} = \boldsymbol{\varphi}, \tilde{\boldsymbol{\tau}} = \mathbf{C}^0 \boldsymbol{\tau}, \tag{A-7}$$

where $\tilde{\boldsymbol{\varphi}}$ and $\tilde{\boldsymbol{\tau}}$ are the transformed adjoint particle velocity vector and stress vector, respectively. Inserting Eq. (A-7) into Eq. (A-6) and applying some basic matrix operations lead to the following adjoint-state equation:

$$\begin{cases} -\rho^0 \dfrac{\partial \tilde{\boldsymbol{\varphi}}}{\partial t} + \mathbf{D}\tilde{\boldsymbol{\tau}} = \mathscr{R}^\dagger \Delta\mathbf{d}_{\mathrm{v}}, \\ -\dfrac{\partial \tilde{\boldsymbol{\tau}}}{\partial t} + \mathbf{C}^0\mathbf{D}^{\mathrm{T}} \tilde{\boldsymbol{\varphi}} = \mathrm{C}^0 \mathscr{R}^\dagger \Delta\mathbf{d}_{\mathrm{p}}. \end{cases} \tag{A-8}$$

Now, the adjoint-state equation resembles the state Eq. (9). The advantage of this reformulation is that it allows us to reuse the forward wave equation solver to solve the adjoint wave equation. The adjoint variables in the original coordinate system are obtained by

$$\boldsymbol{\varphi} = \tilde{\boldsymbol{\varphi}}, \boldsymbol{\tau} = \left(\mathbf{C}^0\right)^{-1} \tilde{\boldsymbol{\tau}}. \tag{A-9}$$

According to Eq. (A-3), the gradient in LWI can be computed by the zeros-lag cross-correlation of forward and adjoint wavefields:

$$\begin{aligned} \Delta\rho(\mathbf{x}) &= -\int_0^T \frac{\partial \mathbf{v}^0}{\partial t} \cdot \boldsymbol{\varphi} \mathrm{d}t, \\ \Delta C_{ij}(\mathbf{x}) &= \int_0^T \left(\frac{\partial \mathbf{C}}{\partial C_{ij}} \mathbf{D}^{\mathrm{T}} \mathbf{v}^0\right) \cdot \boldsymbol{\tau} \mathrm{d}t = \int_0^T \left(\frac{\partial \mathbf{C}}{\partial C_{ij}} \mathbf{D}^{\mathrm{T}} \mathbf{v}^0\right) \cdot \left(\mathbf{D}^{\mathrm{T}} \boldsymbol{\psi}\right) \mathrm{d}t, \end{aligned} \tag{A-10}$$

where $\boldsymbol{\psi} = \int_T^t \boldsymbol{\varphi} \mathrm{d}t$ is the adjoint particle displacement field. The model perturbation for density and stiffness matrix elements can be explicitly expressed as

$$\begin{aligned} \Delta\rho(\mathbf{x}) &= -\int_0^T \frac{\partial v_1^0}{\partial t}\varphi_1 + \frac{\partial v_3^0}{\partial t}\varphi_3 \mathrm{d}t, \\ \Delta C_{11}(\mathbf{x}) &= \int_0^T \frac{\partial v_1^0}{\partial x_1}\frac{\partial \psi_1}{\partial x_1} \mathrm{d}t, \\ \Delta C_{13}(\mathbf{x}) &= \int_0^T \frac{\partial v_1^0}{\partial x_1}\frac{\partial \psi_3}{\partial x_3} + \frac{\partial v_3^0}{\partial x_3}\frac{\partial \psi_1}{\partial x_1} \mathrm{d}t, \\ \Delta C_{33}(\mathbf{x}) &= \int_0^T \frac{\partial v_3^0}{\partial x_3}\frac{\partial \psi_3}{\partial x_3} \mathrm{d}t, \\ \Delta C_{55}(\mathbf{x}) &= \int_0^T \left(\frac{\partial v_1^0}{\partial x_3} + \frac{\partial v_3^0}{\partial x_1}\right)\left(\frac{\partial \psi_1}{\partial x_3} + \frac{\partial \psi_3}{\partial x_1}\right) \mathrm{d}t, \end{aligned} \tag{A-11}$$

where ψ_1 and ψ_3 are horizontal and vertical components of the adjoint particle displacement field:

$$\begin{aligned} \psi_1(\mathbf{x}, t) &= \int_T^t \varphi_1(\mathbf{x}, t) \mathrm{d}t, \\ \psi_3(\mathbf{x}, t) &= \int_T^t \varphi_3(\mathbf{x}, t) \mathrm{d}t. \end{aligned} \tag{A-12}$$

We parametrize the LWI in terms of relative perturbations of vertical velocity and Thomsen parameter ($\Delta\rho/\rho, \Delta V_{\mathrm{p0}}/V_{\mathrm{p0}}, \Delta V_{\mathrm{s0}}/V_{\mathrm{s0}}, \Delta\epsilon, \Delta\delta$) with respect to reference model (Podgornova et al., 2018). We transform the model parameter perturbations using the following equations derived from chain rule in calculus:

$$\begin{pmatrix} \dfrac{\Delta\rho}{\rho} \\ \dfrac{\Delta V_{\mathrm{p0}}}{V_{\mathrm{p0}}} \\ \dfrac{\Delta V_{\mathrm{s0}}}{V_{\mathrm{s0}}} \\ \Delta\epsilon \\ \Delta\delta \end{pmatrix} = \begin{pmatrix} \rho & (1+2\epsilon)\rho V_{\mathrm{p0}}^2 & \rho M - \rho V_{\mathrm{s0}}^2 & \rho V_{\mathrm{p0}}^2 & \rho V_{\mathrm{s0}}^2 \\ 0 & 2(1+2\epsilon)\rho V_{\mathrm{p0}}^2 & \dfrac{M_1}{M} & 2\rho V_{\mathrm{p0}}^2 & 0 \\ 0 & 0 & \dfrac{M_2}{M} - 2\rho V_{\mathrm{s0}}^2 & 0 & 2\rho V_{\mathrm{s0}}^2 \\ 0 & 2\rho V_{\mathrm{p0}}^2 & 0 & 0 & 0 \\ 0 & 0 & \dfrac{M_3}{M} & 0 & 0 \end{pmatrix} \times \begin{pmatrix} \Delta\rho \\ \Delta C_{11} \\ \Delta C_{13} \\ \Delta C_{33} \\ \Delta C_{55} \end{pmatrix}, \tag{A-13}$$

where M_1, M_2, M_3 and M are defined in Eq. (18).

Appendix B

Radiation patterns of VTI-elastic scatters

In this section, we derive the expressions of radiation patterns of VTI-elastic scatters using the Born approximation and high-frequency, far-field asymptotic Green's function. To make the notations more concise, we will derive the following equations in frequency domain. However, one should note that the implementation of our algorithm is in time domain. The equation of motion in general anisotropic elastic media is as follows (Aki and Richards, 2002):

$$\rho\omega^2 u_i + \left(c_{ijkl}u_{k,l}\right)_{,j} = -f_i, \quad i,j,k,l = 1,2,3 \tag{B-1}$$

with appropriate boundary conditions. In the above equation, u_i is the particle displacement, c_{ijkl} is stiffness tensor, f_i is source term, ω is the circular frequency, subscript $(,j)$ denotes the partial derivative $\partial/\partial x_j$, and Einstein's summation convention is used. The elastodynamic Green's function is a solution of the equation:

$$\rho\omega^2 G_{in} + \left(c_{ijkl}G_{kn,l}\right)_{,j} = -\delta_{in}\delta(\mathbf{x}-\mathbf{x}'), \tag{B-2}$$

where Green's function $G_{in}(\mathbf{x},\mathbf{x}',\omega)$ represents the i th component of the displacement vector at location $\mathbf{x}$ dues to the unit impulse applied at $\mathbf{x}'$ in the n-direction, $\delta(\mathbf{x})$ is Dirac delta function, δ_{in} is Kronecker symbol. The particle displacement can be expressed in terms of Green's function using the representation theorem:

$$u_n(\mathbf{x},\omega) = \int_V G_{ni}(\mathbf{x},\mathbf{x}',\omega) f_i(\mathbf{x}',\omega)\mathrm{d}V(\mathbf{x}'). \tag{B-3}$$

The Born approximation for general anisotropic elastic wave equation can be written as

$$\rho^0\omega^2\Delta u_i + \left(c^0_{ijkl}\Delta u_{k,l}\right)_{,j} = -\Delta\rho\omega^2 u^0_i - \left(\Delta c_{ijkl}u^0_{k,l}\right)_{,j}, \tag{B-4}$$

where ρ^0, c^0_{ijkl} are reference density and stiffness coefficient, u^0_i is particle displacement in reference model, $\Delta\rho$ and Δc_{ijkl} are the density and stiffness coefficient perturbations and Δu_i is the particle displacement perturbation. Using the representation theorem, the data perturbation can be written as

$$\begin{aligned}\Delta u_n(\mathbf{x}_r,\omega) = &\int_V f_m(\mathbf{x}_s,\omega)\Delta\rho(\mathbf{x})\omega^2 G^0_{mi}(\mathbf{x}_s,\mathbf{x},\omega)\tilde{G}^0_{ni}(\mathbf{x}_r,\mathbf{x},\omega)\mathrm{d}V(\mathbf{x})\\ &-\int_V f_m(\mathbf{x}_s,\omega)\Delta c_{ijkl}(\mathbf{x})G^0_{mk,l}(\mathbf{x}_s,\mathbf{x},\omega)\tilde{G}^0_{ni,j}(\mathbf{x}_r,\mathbf{x},\omega)\mathrm{d}V(\mathbf{x}),\end{aligned} \tag{B-5}$$

where $G^0_{mi}(\mathbf{x}_s,\mathbf{x},\omega)$ and $\tilde{G}^0_{ni}(\mathbf{x}_r,\mathbf{x},\omega)$ are the source-side and receiver-side Green's function in reference media, respectively. From now on, the tilde $(\tilde{})$ superscript is used to indicate quantities associated with scattered wavefield (receiver-side). The source-side, high-frequency, far-field asymptotic Green's function for anisotropic elastic media can be written as (Červený, 2001):

$$G^0_{mk}(\mathbf{x}_s,\mathbf{x},\omega) = \sum_\Omega \frac{g_m g_k}{4\pi\rho V_g r\sqrt{|K|}} e^{i\omega\mathbf{p}\cdot\mathbf{r}/V}, \tag{B-6}$$

where V_g is group velocity, K is the Gaussian curvature of the slowness surface, $\mathbf{g}$ is unit polarization vector, V is the phase velocity, $\mathbf{p}$ is the unit slowness vector, $\mathbf{r} = (\mathbf{x}_s - \mathbf{x})$, $r = |\mathbf{r}|$ and Ω indicates the type of body wave. Inserting Eq. (B-6) into scattering integral Eq. (B-5), one can arrive

$$\Delta u_n(\mathbf{x}_r,\omega) = \sum_\Omega \int_V \frac{f_m\omega^2 g_m\tilde{g}_n}{(4\pi\rho)^2(V_g rV)(\tilde{V}_g\tilde{r}\tilde{V})|K|}\left(\Delta\rho V\tilde{V}g_i\tilde{g}_i + \Delta c_{ijkl}g_k\tilde{g}_i p_l\tilde{p}_j\right)e^{i\omega\tau}\mathrm{d}V(\mathbf{x}) \tag{B-7}$$

where $\tau = (\mathbf{p}\bullet\mathbf{r}/V + \tilde{\mathbf{p}}\bullet\tilde{\mathbf{r}}/\tilde{V})$ is traveltime from source to receiver, the summation over Ω is for different scatter wave types (nine types for 3D case and four types for 2D case). The terms inside the parentheses of the integrand are the scattering function for an arbitrarily anisotropic scatter embedded in a homogeneous anisotropic background model:

$$R = \Delta\rho V\tilde{V}g_i\tilde{g}_i + \Delta c_{ijkl}g_k\tilde{g}_i p_l\tilde{p}_j, \tag{B-8}$$

The scattering function equals to the product of radiation pattern and model perturbation. We consider scattering radiation patterns due to perturbations of elastic stiffnesses in vertical transversely isotropic medium. Without losing generality, we consider coordinate system with x_3 axis aligned with the vertical symmetric axis and the x_1 axis coplanar with the sources and receivers. The Voigt notation can be used to rewrite the elastic stiffness tensor c_{ijkl} to reduced order stiffness matrix C_{ij}. In 2D case, the P and SV waves are polarized in $x_1 - x_3$ plane and quantities in x_2 direction are equal to zero:

$$p_2 = \tilde{p}_2 = 0, g_2 = \tilde{g}_2 = 0. \tag{B-9}$$

Then, the 2D scattering radiation patterns can be written as

$$\begin{cases} \Gamma^{AB}_{\Delta\rho} = V^A\tilde{V}^B\left(g^A_1\tilde{g}^B_1 + g^A_3\tilde{g}^B_3\right),\\ \Gamma^{AB}_{\Delta C_{11}} = p^A_1\tilde{p}^B_1 g^A_1\tilde{g}^B_1,\\ \Gamma^{AB}_{\Delta C_{13}} = p^A_1\tilde{p}^B_3 g^A_1\tilde{g}^B_3 + p^A_3\tilde{p}^B_1 g^A_3\tilde{g}^B_1,\\ \Gamma^{AB}_{\Delta C_{33}} = p^A_3\tilde{p}^B_3 g^A_3\tilde{g}^B_3,\\ \Gamma^{AB}_{\Delta C_{55}} = \left(p^A_1 g^A_3 + p^A_3 g^A_1\right)\left(\tilde{p}^B_1\tilde{g}^B_3 + \tilde{p}^B_3\tilde{g}^B_1\right), \end{cases} \tag{B-10}$$

where Γ is radiation pattern of a particular parameter, A and B are wave mode type indices (P or SV wave). The polarization vector and slowness vector are dependent on the Green's function in reference model and can be computed numerically. To obtain analytical scattering radiation patterns, we further assume that the elastic reference medium is isotropic. The unit slowness vector $\mathbf{p}$ is parallel to the ray direction, and the polarization vector $\mathbf{g}$ is parallel or perpendicular to the ray direction. For P–P reflection wave, the unit

slowness vector and unit polarization vector can be expressed using the incident and reflection angle of P–P wave:

$$\begin{aligned} &p_1^{\mathrm{P}} = -\sin\theta_{\mathrm{p}}, p_3^{\mathrm{P}} = \cos\theta_{\mathrm{p}}, \tilde{p}_1^{\mathrm{P}} = \sin\theta_{\mathrm{p}}, \tilde{p}_3^{\mathrm{P}} = \cos\theta_{\mathrm{p}}, \\ &g_1^{\mathrm{P}} = p_1^{\mathrm{P}}, g_3^{\mathrm{P}} = p_3^{\mathrm{P}}, \tilde{g}_1^{\mathrm{P}} = \tilde{p}_1^{\mathrm{P}}, \tilde{g}_3^{\mathrm{P}} = \tilde{p}_3^{\mathrm{P}}, \end{aligned} \tag{B-11}$$

where θ_{p} is the incident angle of P-wave (the angle that the direction of incident P-wave makes with the x_3 axis). The radiation patterns of VTI-elastic scatters for P–P reflection wave are

$$\begin{cases} \Gamma^{\mathrm{PP}}_{\Delta\rho} = V_{\mathrm{p0}}^2\left(-\sin^2\theta_{\mathrm{p}} + \cos^2\theta_{\mathrm{p}}\right), \\ \Gamma^{\mathrm{PP}}_{\Delta C_{11}} = \sin^4\theta_{\mathrm{p}}, \\ \Gamma^{\mathrm{PP}}_{\Delta C_{13}} = 2\sin^2\theta_{\mathrm{p}}\cos^2\theta_{\mathrm{p}}, \\ \Gamma^{\mathrm{PP}}_{\Delta C_{33}} = \cos^4\theta_{\mathrm{p}}, \\ \Gamma^{\mathrm{PP}}_{\Delta C_{55}} = -4\sin^2\theta_{\mathrm{p}}\cos^2\theta_{\mathrm{p}}, \end{cases} \tag{B-12}$$

and

$$\begin{cases} \Gamma^{\mathrm{PP}}_{\Delta\rho/\rho} = 2 - 2\sin^2\theta_{\mathrm{p}} - 2V_{\mathrm{sp}}^2\sin^2 2\theta_{\mathrm{p}}, \\ \Gamma^{\mathrm{PP}}_{\Delta V_{\mathrm{p0}}/V_{\mathrm{p0}}} = 2, \\ \Gamma^{\mathrm{PP}}_{\Delta V_{\mathrm{s0}}/V_{\mathrm{s0}}} = -4V_{\mathrm{sp}}^2\sin^2 2\theta_{\mathrm{p}}, \\ \Gamma^{\mathrm{PP}}_{\Delta\epsilon} = 2\sin^4\theta_{\mathrm{p}}, \\ \Gamma^{\mathrm{PP}}_{\Delta\delta} = \frac{1}{2}\sin^2 2\theta_{\mathrm{p}}, \end{cases} \tag{B-13}$$

where $V_{\mathrm{sp}} = V_{\mathrm{s0}}/V_{\mathrm{p0}}$ is the ratio of vertical S- and P-wave velocities in the reference medium. The radiation patterns of $(\Delta\rho/\rho, \Delta V_{\mathrm{p0}}/V_{\mathrm{p0}}, \Delta V_{\mathrm{s0}}/V_{\mathrm{s0}}, \Delta\epsilon, \Delta\delta)$ are obtained from radiation patterns of $(\Delta\rho, \Delta C_{11}, \Delta C_{13}, \Delta C_{33}, \Delta C_{55})$ via parameter transformation using Eq. (A-13). For P–S reflection wave, the unit slowness vector and unit polarization vector can be written using the incident and reflection angle of P–S wave:

$$\begin{aligned} &p_1^{\mathrm{P}} = -\sin\theta_{\mathrm{p}}, p_3^{\mathrm{P}} = \cos\theta_{\mathrm{p}}, \tilde{p}_1^{\mathrm{S}} = \sin\theta_{\mathrm{s}}, \tilde{p}_3^{\mathrm{S}} = \cos\theta_{\mathrm{s}}, \\ &g_1^{\mathrm{P}} = p_1^{\mathrm{P}}, g_3^{\mathrm{P}} = p_3^{\mathrm{P}}, \tilde{g}_1^{\mathrm{S}} = \tilde{p}_3^{\mathrm{S}}, \tilde{g}_3^{\mathrm{S}} = -\tilde{p}_1^{\mathrm{S}}, \end{aligned} \tag{B-14}$$

where θ_{s} is the scattering angle of S-wave (the angle that the direction of scattered S-wave makes with the x_3 axis). The radiation patterns of VTI-elastic scatters for P–S reflection wave are

$$\begin{cases} \Gamma^{\mathrm{PS}}_{\Delta\rho} = -V_{\mathrm{p0}}V_{\mathrm{s0}}\sin(\theta_{\mathrm{p}} + \theta_{\mathrm{s}}), \\ \Gamma^{\mathrm{PS}}_{\Delta C_{11}} = \frac{1}{2}\sin 2\theta_{\mathrm{s}}\sin^2\theta_{\mathrm{p}}, \\ \Gamma^{\mathrm{PS}}_{\Delta C_{13}} = \frac{1}{2}\sin 2\theta_{\mathrm{s}}\cos 2\theta_{\mathrm{p}}, \\ \Gamma^{\mathrm{PS}}_{\Delta C_{33}} = -\frac{1}{2}\sin 2\theta_{\mathrm{s}}\cos^2\theta_{\mathrm{p}}, \\ \Gamma^{\mathrm{PS}}_{\Delta C_{55}} = -\sin 2\theta_{\mathrm{p}}\cos 2\theta_{\mathrm{s}}, \end{cases} \tag{B-15}$$

and

$$\begin{cases} \Gamma^{\mathrm{PS}}_{\Delta\rho/\rho} = -\sin(\theta_{\mathrm{p}} + \theta_{\mathrm{s}}) - V_{\mathrm{sp}}\sin 2(\theta_{\mathrm{p}} + \theta_{\mathrm{s}}), \\ \Gamma^{\mathrm{PS}}_{\Delta V_{\mathrm{p0}}/V_{\mathrm{p0}}} = 0, \\ \Gamma^{\mathrm{PS}}_{\Delta V_{\mathrm{s0}}/V_{\mathrm{s0}}} = -2V_{\mathrm{sp}}\sin 2(\theta_{\mathrm{p}} + \theta_{\mathrm{s}}), \\ \Gamma^{\mathrm{PS}}_{\Delta\epsilon} = V_{\mathrm{ps}}\sin 2\theta_{\mathrm{s}}\sin^2\theta_{\mathrm{p}}, \\ \Gamma^{\mathrm{PS}}_{\Delta\delta} = \frac{1}{2}V_{\mathrm{ps}}\cos 2\theta_{\mathrm{p}}\sin 2\theta_{\mathrm{s}}, \end{cases} \tag{B-16}$$

where $V_{\mathrm{ps}} = V_{\mathrm{p0}}/V_{\mathrm{s0}}$. For S–S reflection wave, the unit slowness vector and unit polarization vector have the following relationship:

$$\begin{aligned} &p_1^{\mathrm{S}} = -\sin\theta_{\mathrm{s}}, p_3^{\mathrm{S}} = \cos\theta_{\mathrm{s}}, \tilde{p}_1^{\mathrm{S}} = \sin\theta_{\mathrm{s}}, \tilde{p}_3^{\mathrm{S}} = \cos\theta_{\mathrm{s}}, \\ &g_1^{\mathrm{S}} = p_3^{\mathrm{S}}, g_3^{\mathrm{S}} = -p_1^{\mathrm{S}}, \tilde{g}_1^{\mathrm{S}} = \tilde{p}_3^{\mathrm{S}}, \tilde{g}_3^{\mathrm{S}} = -\tilde{p}_1^{\mathrm{S}}, \end{aligned} \tag{B-17}$$

The radiation patterns of VTI-elastic scatters for S–S reflection wave are

$$\begin{cases} \Gamma^{\mathrm{SS}}_{\Delta\rho} = -V_{\mathrm{s0}}^2\cos 2\theta_{\mathrm{s}}, \\ \Gamma^{\mathrm{SS}}_{\Delta C_{11}} = -\frac{1}{4}\sin^2 2\theta_{\mathrm{s}}, \\ \Gamma^{\mathrm{SS}}_{\Delta C_{13}} = \frac{1}{2}\sin^2 2\theta_{\mathrm{s}}, \\ \Gamma^{\mathrm{SS}}_{\Delta C_{33}} = -\frac{1}{4}\sin^2 2\theta_{\mathrm{s}}, \\ \Gamma^{\mathrm{SS}}_{\Delta C_{55}} = \cos^2 2\theta_{\mathrm{s}}, \end{cases} \tag{B-18}$$

and

$$\begin{cases} \Gamma^{\mathrm{SS}}_{\Delta\rho/\rho} = \cos 2\theta_{\mathrm{s}} + \cos 4\theta_{\mathrm{s}}, \\ \Gamma^{\mathrm{SS}}_{\Delta V_{\mathrm{p0}}/V_{\mathrm{p0}}} = 0, \\ \Gamma^{\mathrm{SS}}_{\Delta V_{\mathrm{s0}}/V_{\mathrm{s0}}} = 2\cos 4\theta_{\mathrm{s}}, \\ \Gamma^{\mathrm{SS}}_{\Delta\epsilon} = -\frac{1}{2}V_{\mathrm{ps}}^2\sin^2 2\theta_{\mathrm{s}}, \\ \Gamma^{\mathrm{SS}}_{\Delta\delta} = \frac{1}{2}V_{\mathrm{ps}}^2\sin^2 2\theta_{\mathrm{s}}. \end{cases} \tag{B-19}$$

In Fig. 19, we plot the scattering radiation patterns of perturbations of VTI-elastic parameters $(\Delta\rho/\rho, \Delta V_{\mathrm{p0}}/V_{\mathrm{p0}}, \Delta V_{\mathrm{s0}}/V_{\mathrm{s0}}, \Delta\epsilon, \Delta\delta)$ in isotropic elastic reference medium. The scattering radiation patterns are plotted in polar coordinates as a function of the scattering angle (open angle between incident and scattered wave). Scattering radiation patterns for different elastic parameters overlap and cause the so-called crosstalk artifacts in waveform inversion. The scattering radiation patterns of Thomsen anisotropy parameters have smaller amplitude comparing with the ones of vertical velocities. The Thomsen anisotropy parameters are mainly sensitive to intermediate to large scattering angles.

References

Aki, K., Richards, P.G., 2002. Quantitative Seismology. University Science Books, California, USA.

Anikiev, D., Kashtan, B., Mulder, W.A., 2013. Decoupling of elastic parameters with iterative linearized inversion. In: 83rd Annual International Meeting. SEG, Expanded Abstracts, pp. 3185–3190. https://doi.org/10.1190/segam2013-0904.1.

Bourgeois, A., Jiang, B.F., Lailly, P., 1989. Linearized inversion: a significant step beyond pre-stack migration. Geophys. J. Int. 99 (2), 435–445. https://doi.org/10.1111/j.1365-246X.1989.tb01700.x.

Červený, V., 2001. Seismic Ray Theory. Cambridge University Press, Cambridge, UK.

Chen, K., Sacchi, M.D., 2017. Elastic least-squares reverse time migration via

linearized elastic full-waveform inversion with pseudo-hessian preconditioning. Geophysics 82 (5), S341–S358. https://doi.org/10.1190/geo2016-0613.1.
Chen, K., Sacchi, M.D., 2018. The importance of including density in elastic least-squares reverse time migration. Multiparameter crosstalk and convergence. Geophys. J. Int. 216 (1), 61–80. https://doi.org/10.1093/gji/ggy368.
Chen, K., Liu, L., Zhang, L., et al., 2023. Vertical transversely isotropic elastic least-squares reverse time migration based on elastic wavefield vector decomposition. Geophysics 88 (1), S27–S45. https://doi.org/10.1190/geo2022-0068.1.
Cheng, J., Fomel, S., 2014. Fast algorithms for elastic-wave-mode separation and vector decomposition using low-rank approximation for anisotropic media. Geophysics 79 (4), C97–C110. https://doi.org/10.1190/geo2014-0032.1.
Du, Q., Zhu, Y., Ba, J., 2012. Polarity reversal correction for elastic reverse time migration. Geophysics 77 (2), S31–S41. https://doi.org/10.1190/geo2011-0348.1.
Duan, Y., Guitton, A., Sava, P., 2017. Elastic least-squares reverse time migration. Geophysics 82 (4), S315–S325. https://doi.org/10.1190/geo2016-0564.1.
Fang, J., Zhou, H., Chen, H., et al., 2019. Source-independent elastic least-squares reverse time migration. Geophysics 84 (1), S1–S16. https://doi.org/10.1190/geo2017-0847.1.
Feng, Z., Schuster, G.T., 2017. Elastic least-squares reverse time migration. Geophysics 82 (2), S143–S157. https://doi.org/10.1190/geo2016-0254.1.
Gu, B., Li, Z., Yang, P., et al., 2017. Elastic least-squares reverse time migration with hybrid l1/l2 misfit function. Geophysics 82 (3), S271–S291. https://doi.org/10.1190/geo2016-0235.1.
Gu, B., Han, J., Ren, Z., et al., 2019. 2D least-squares elastic reverse time migration of multicomponent seismic data. Geophysics 84 (6), S523–S538. https://doi.org/10.1190/geo2018-0720.1.
Gu, B., Huang, J., Han, J., et al., 2021. Least-squares inversion-based elastic reverse time migration with PP- and PS-angle-domain common-imaging gathers. Geophysics 86 (1), S29–S44. https://doi.org/10.1190/geo2020-0028.1.
Guitton, A., Alkhalifah, T., 2017. A parameterization study for elastic VTI full-waveform inversion of hydrophone components: synthetic and North Sea field data examples. Geophysics 82 (6), R299–R308. https://doi.org/10.1190/geo2017-0073.1.
He, W., Plessix, R.E., Singh, S., 2018. Parametrization study of the land multiparameter VTI elastic waveform inversion. Geophys. J. Int. 213 (3), 1660–1672. https://doi.org/10.1093/gji/ggy099.
Huang, J., Li, Z., Kong, X., et al., 2013. A study of least-squares migration imaging method for fractured-type carbonate reservoir. Chin. J. Geophys. 56 (5), 1716–1725. https://doi.org/10.6038/cjg20130529 (in Chinese).
Kamath, N., Tsvankin, I., 2016. Elastic full-waveform inversion for VTI media: Methodology and sensitivity analysis. Geophysics 81 (2), C53–C68. https://doi.org/10.1190/geo2014-0586.1.
Kamath, N., Tsvankin, I., Diaz, E., 2017. Elastic full-waveform inversion for VTI media: a synthetic parameterization study. Geophysics 82 (5), C163–C174. https://doi.org/10.1190/geo2016-0375.1.
Kang, W., Cheng, J., 2012. Methods of suppressing artifacts in prestack reverse time migration. Prog. Geophys. 27 (3), 1163–1172. https://doi.org/10.6038/j.issn.1004-2903.2012.03.041.
Kohn, D., 2011. Time Domain 2D Elastic Full Waveform Tomography. Ph.D. thesis, Christian-Albrechts-Universitat zu Kiel.
Kuehl, H., Sacchi, M.D., 2003. Least-squares wave-equation migration for AVP/AVA inversion. Geophysics 68 (1), 262–273. https://doi.org/10.1190/1.1543212.
Li, Z., Ma, X., Fu, C., et al., 2016. Wavefield separation and polarity reversal correction in elastic reverse time migration. J. Appl. Geophys. 127, 56–67. https://doi.org/10.1016/j.jappgeo.2016.02.012.
Lambaré, G., Virieux, J., Madariaga, R., et al., 1992. Iterative asymptotic inversion in the acoustic approximation. Geophysics 57 (9), 1138–1154. https://doi.org/10.1190/1.1443328.
Li, C., Huang, J., Li, Z., et al., 2018. Plane-wave least-squares reverse time migration with a preconditioned stochastic conjugate gradient method. Geophysics 83 (1), S33–S46. https://doi.org/10.1190/geo2017-0339.1.
Liu, Y., Huang, X., Wan, X., et al., 2019. Elastic multi-parameter full-waveform inversion for anisotropic media. Chin. J. Geophys. 62 (5), 1809–1823. https://doi.org/10.6038/cjg2019M0176 (in Chinese).
Lu, S., Li, X., Valenciano, A., et al., 2017. Least-squares wave-equation migration for broadband imaging. In: 79th EAGE Conference & Exhibition. European Association of Geoscientists & Engineers, pp. 1–5. https://doi.org/10.3997/2214-4609.201700803.
Lu, Y., Liu, Q., Zhang, J., et al., 2019. Poynting and polarization vectors based wavefield decomposition and their application on elastic reverse time migration in 2D transversely isotropic media. Geophys. Prospect. 67 (5), 1296–1311. https://doi.org/10.1111/1365-2478.12777.
Mu, X., Huang, J., Yang, J., et al., 2020. Least-squares reverse time migration in TTI media using a pure qP-wave equation. Geophysics 85 (4), S199–S216. https://doi.org/10.1190/geo2019-0320.1.
Musgrave, M., 2003. Crystal Acoustics: Introduction to the Study of Elastic Waves and Vibrations in Crystals. Acoustical Society of America.
Nemeth, T., Wu, C., Schuster, G.T., 1999. Least-squares migration of incomplete reflection data. Geophysics 64 (1), 208–221. https://doi.org/10.1190/1.1444517.
Paige, C.C., Saunders, M.A., 1982. LSQR: an algorithm for sparse linear equations and sparse least squares. ACM Trans. Math Software 8 (1), 43–71. https://doi.org/10.1145/355984.355989.
Pan, W., Innanen, K.A., Margrave, G.F., et al., 2016. Estimation of elastic constants for HTI media using Gauss-Newton and full-Newton multiparameter full-waveform inversion. Geophysics 81 (5), R275–R291. https://doi.org/10.1190/geo2015-0594.1.
Pan, W., Innanen, K.A., Wang, Y., 2020. Parameterization analysis and field validation of VTI-elastic full-waveform inversion in a walk-away vertical seismic profile configuration. Geophysics 85 (3), B87–B107. https://doi.org/10.1190/geo2019-0089.1.
Podgornova, O., Leaney, S., Liang, L., 2018. Resolution of VTI anisotropy with elastic full-waveform inversion: theory and basic numerical examples. Geophys. J. Int. 214 (1), 200–218. https://doi.org/10.1093/gji/ggy116.
Qu, Y., Huang, C., Liu, C., et al., 2019. Multiparameter least-squares reverse time migration for acoustic-elastic coupling media based on ocean bottom cable data. Appl. Geophys. 16 (3), 327–337. https://doi.org/10.1007/s11770-019-0771-4.
Ren, Z., Liu, Y., Sen, M.K., 2017. Least-squares reverse time migration inelastic media. Geophys. J. Int. 208 (2), 1103–1125. https://doi.org/10.1093/gji/ggw443.
Stanton, A., Sacchi, M.D., 2017. Elastic least-squares one-way wave-equation migration. Geophysics 82 (4), S293–S305. https://doi.org/10.1190/geo2016-0391.1.
Østmo, S., Mulder, W.A., Plessix, R.-E., 2002. Finite-difference iterative migration by linearized waveform inversion in the frequency domain. In: 72nd Annual International Meeting. SEG, Expanded Abstracts, pp. 1384–1387. https://doi.org/10.1190/1.1816917.
Stolt, R.H., Weglein, A.B., 2012. Seismic Imaging and Inversion: Application of Linear Inverse Theory. Cambridge University Press, Cambridge, USA.
Sun, M., Dong, L., Yang, J., et al., 2018. Elastic least-squares reverse time migration with density variations. Geophysics 83 (6), S533–S547. https://doi.org/10.1190/geo2017-0517.1.
Tarantola, A., 1984. Linearized inversion of seismic reflection data. Geophys. Prospect. 32 (6), 998–1015. https://doi.org/10.1111/j.1365-2478.1984.tb00751.x.
Thomsen, L., 1986. Weak elastic anisotropy. Geophysics 51 (10), 1954–1966. https://doi.org/10.1190/1.1442051.
Virieux, J., Operto, S., 2009. An overview of full-waveform inversion in exploration geophysics. Geophysics 74 (6), WCC1–WCC26. https://doi.org/10.1190/1.3238367.
Wang, X., Zhang, J., 2022. Fast wave-mode separation in anisotropic elastic reverse time migration using the phase velocity-related Poynting vector. J. Comput. Phys. 461, 111200. https://doi.org/10.1016/j.jcp.2022.111200.
Wang, C., Cheng, J., Arntsen, B., 2016. Scalar and vector imaging based on wave mode decoupling for elastic reverse time migration in isotropic and transversely isotropic media. Geophysics 81 (5), S383–S398. https://doi.org/10.1190/geo2015-0704.1.
Wang, X., Lu, Y., Zhang, J., 2021. Elastic wave-mode separation in 2D transversely isotropic media using optical flow. Geophys. Prospect. 69 (2), 349–371. https://doi.org/10.1111/1365-2478.13061.
Xu, L., Stanton, A., Sacchi, M.D., 2016. Elastic least-squares reverse time migration. In: 86th Annual International Meeting. SEG, Expanded Abstracts, pp. 2289–2293. https://doi.org/10.1190/segam2016-13962459.1.
Yan, J., Sava, P., 2008. Isotropic angle-domain elastic reverse-time migration. Geophysics 73 (6), S229–S239. https://doi.org/10.1190/1.2981241.
Yang, J., Liu, Y., Dong, L., 2016. Least-squares reverse time migration in the presence of density variations. Geophysics 81 (6), S497–S509. https://doi.org/10.1190/geo2016-0075.1.
Yang, J., Zhu, H., Wang, W., et al., 2018a. Isotropic elastic reverse time migration using the phase- and amplitude-corrected vector P- and S-wavefields. Geophysics 83 (6), S489–S503. https://doi.org/10.1190/geo2018-0023.1.
Yang, P., Brossier, R., Metivier, L., et al., 2018b. A time-domain preconditioned truncated Newton approach to visco-acoustic multiparameter full waveform inversion. SIAM J. Sci. Comput. 40 (4), B1101–B1130. https://doi.org/10.1137/17M1126126.
Yang, J., Zhang, H., Zhao, Y., et al., 2019a. Elastic wavefield separation in anisotropic media based on eigenform analysis and its application in reverse-time migration. Geophys. J. Int. 217 (2), 1290–1313. https://doi.org/10.1093/gji/ggz085.
Yang, J., Zhu, H., McMechan, G., et al., 2019b. Elastic least-squares reverse time migration in vertical transverse isotropic media. Geophysics 84 (6), S539–S553. https://doi.org/10.1190/geo2018-0887.1.
Yang, J., Hua, B., Williamson, P., et al., 2020. Elastic least-squares imaging in tilted transversely isotropic media for multicomponent land and pressure marine data. Surv. Geophys. 41 (4), 805–833. https://doi.org/10.1007/s10712-020-09588-3.
Yao, G., Jakubowicz, H., 2016. Least-squares reverse-time migration in a matrix-based formulation. Geophys. Prospect. 64 (3), 611–621. https://doi.org/10.1111/1365-2478.12305.
Zhang, Q., McMechan, G.A., 2010. 2D and 3D elastic wavefield vector decomposition in the wavenumber domain for VTI media. Geophysics 75 (3), D13–D26. https://doi.org/10.1190/1.3431045.
Zhang, W., Shi, Y., 2019. Imaging conditions for elastic reverse time migration. Geophysics 84 (2), S95–S111. https://doi.org/10.1190/geo2018-0197.1.
Zhang, L., Liu, L., Niu, F., et al., 2022. A novel and efficient engine for P-/S-wave-mode vector decomposition for vertical transverse isotropic elastic reverse time migration. Geophysics 87 (4), S185–S207. https://doi.org/10.1190/geo2021-0609.1.
Zhong, Y., Gu, H., Liu, Y., et al., 2021. Elastic reverse-time migration with complex topography. Energies 14 (23), 7837. https://doi.org/10.3390/en14237837.
Zhong, Y., Gu, H., Liu, Y., et al., 2022. Elastic reverse time migration method in vertical transversely isotropic media including surface topography. Geophys. Prospect. 70 (9), 1528–1555. https://doi.org/10.1111/1365-2478.13261.
Zuo, J., Niu, F., Liu, L., et al., 2022. 3D anisotropic P- and S-mode wavefields separation in 3D elastic reverse-time migration. Surv. Geophys. 43 (3), 673–701. https://doi.org/10.1007/s10712-021-09688-8.